ATOMIC SCALE DETAILS OF DEDECT-BOUNDARY INTERACTIONS

A Thesis

by

DI CHEN

Submitted to the Office of Graduate and Professional Studies of
Texas A&M University
in partial fulfillment of the requirements for the degree of

DOCTOR OF PHILOSOPHY

Chair of Committee,   Lin Shao
Committee Members,   Tahir Cagin
                     Karl T. Hartwig
                     Jim E. Morel
Head of Department,   Yassin Hassan

December 2014

Major Subject: Nuclear Engineering

ABSTRACT

The study is aimed to understand atomic scale details of defect-boundary interactions, which are critical to develop radiation tolerant fuel cladding materials for harsher neutron environments. By means of molecular dynamics simulations, we addressed the key questions of (1) how defects are trapped by a grain boundary, (2) how defect are annihilated at a grain boundary, and (3) what are upper limits of radiation tolerance of boundary-engineered metals. The modeling is performed by using large-scale atomic/molecular massively parallel simulator (LAMMPS) code and pure Fe is selected as the model material.

For mechanism of defect tapping towards a grain boundary, we find that, instead of the general consensus that the trapping is caused by biased defect diffusions due to relatively lower defect formation energies at a grain boundary, long range defect migration is realized by creation of chain like defects. A chain is induced by the stress field around a defect, and is formed by pushing its immediate lattice atom neighbor into an interstitial site. This newly formed interstitial can induce formation of another vacancy-interstitial pair along the chain direction. The process is repeated or simultaneously occurs along the chain. Thus, a chain consists of alternately positioned interstitials and vacancies. The subsequent defect annihilation between neighboring defects on the chain leads to the defect transport. We identify three types of defect transport models which involve different chains.

For mechanism of defect annihilation on a grain boundary, we find that both defect transport and interstitial-vacancy recombination are realized by formation of similar chain-like defects. The vacancy and interstitial along the chain correspond to the sites of their corresponding formation energy minima, thus the capability to form such chains is determined by the patterns of boundary defect formation energies. For a boundary of small misorientation angle, chain formation is allowed to occur in one direction only and all chains are parallel to each other. At large angles, however, chains are so close to each other that new allowable chain directions are created by linking patterns from different chains. This suggests that large angle boundaries are more efficient to move and recombine defects. The modeling further calculates the energy barriers for chain-mediated defect recombination under different boundary configurations.

These findings lead to the conclusion that defect sink strengths of grain boundaries are determined by not only the efficiency to transport to boudnaries, but also the efficiency to recombine boundary defects. Otherwise, the difficulty to remove defects will quickly turn of the sink property. This is confirmed by comparing the width of defect denuded zone created around a boundary, in a cell randomly bombarded by Fe self-ions to different damage levels. A large angle boundary is more preferred to achieve maximum radiation tolerance.

DEDICATION

To my family and my brother

ACKNOWLEDGEMENTS

I would like to thank Dr. Lin Shao my advisor, without whom this thesis would not have been completed. His supervision and encouragement helped me grow as a researcher and person during my time under his advisement.

I would like to thank my committee members, Dr. Tahir Cagin, Dr. Karl T. Hartwig and Dr. Jim E. Morel. I'm very appreciative for you serving as my committee members, supporting me on this journey.

I would also like to thank our lab manager Xuemei Wang and my colleagues, for helping me with my experiments and technical support. We had a good time together and learned a lot from each other.

NOMENCLATURE

GB	Grain-Boudary
BCC	Body -Centered Cubic
EAM	Embedded-Atom Method
Fe	Ferrum
KeV	Kilo electron Volt
LAMMPS	Large-scale Atomic/Molecular Massively Parallel Simulator
MD	Molecular Dynamics
MeV	Mega electron Volt
Nm	Nanometer
PKA	Primary Knock-on Atom
Ps	Picoseconds
SRIM	Stopping and Range of Ion in Matter
ZBL	Ziegler, Littmark and Biersack
FIB	Focused Ion Beam
TEM	Transmission Electron Microscope
SEM	Scanning Electron Microscope
cm	centimeter
mm	millimeter
EAM	Embedded Atom Method
DPA	Displacements Per Atom

CSL	Coincident Site Lattice
NEB	Nudge Elastic Band
SFT	Stacking Fault Tetrahedral
ZBL	Ziegler, Littmark and Biersack

TABLE OF CONTENTS

LIST OF FIGURES

CHAPTER I

INTRODUCTION

Materials used for nuclear reactors are very important for the safe and reliable operation of such a system. Those materials must endure extreme environmental conditions, such as high pressure and temperature, corrosion, and irradiation. For fusion or fission reactors, the in-core structural components can accumulate radiation damage up to 100s of DPA (displacement per atom). Consequently, irradiation caused by high energy particles and fission fragments can create serious damage to the materials atomistic structure. This ion damage will build up and develop into voids, dislocations, and stacking fault defects. This can lead to materials failure through creep, embrittlement, and swelling, which will negatively impact the reactor's safety and reliability.
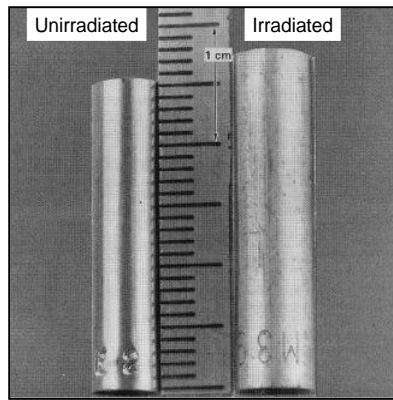
(a)
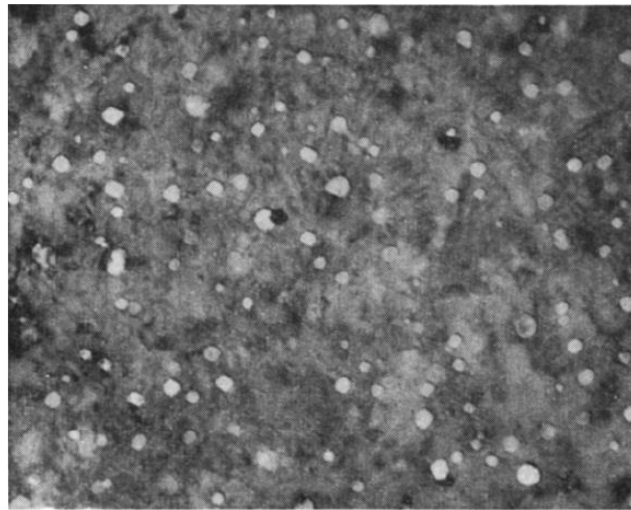
(b)

Fig 1. Dimensional changes and microstructure of stainless steel after high fluence neutron irradiation in a nuclear reactor   (a) Dimensional changes of cold worked 316 stainless steel before and after 1.5×10^{23} m^{-2} neutron irradiation[1] (b) Microstructure of Stainless steel irradiated at 510 ^{o}C to a neutron dose of 4.7×10^{22} cm^{-2}[2]

Take void formation as an example. **Fig** 1. (a) shows the effect of a high neutron fluence on the dimensional changes and microstructure of stainless steel. Significant changes were observed for cold worked 316 stainless steel after 1.5×10^{23} m^{-2} neutron irradiation [1]. This large dimension change might affect its mechanical properties, negatively impacting its ability to perform its intended function. Observe the microstructure shown in **Fig** 1. (b). A large number of voids were found in Stainless steel irradiated at 510 $^{\circ}$C to a neutron dose of 4.7×10^{22} cm^{-2}[2]. Based on these studies, the dimension change is stainless steel caused by neutron irradiation, which has been threatening the safety of nuclear reactors, is largely due to void formation.

Furthermore, next generation advanced reactors require higher temperature and higher fluence in comparison with present day nuclear reactors (see in **Fig** 2.). Creep, embrittlement, and swelling will pose an even more serious problem in these advanced designs. This presents a huge challenge for nuclear materials. As a result, new materials need to be developed that have a high radiation tolerance.
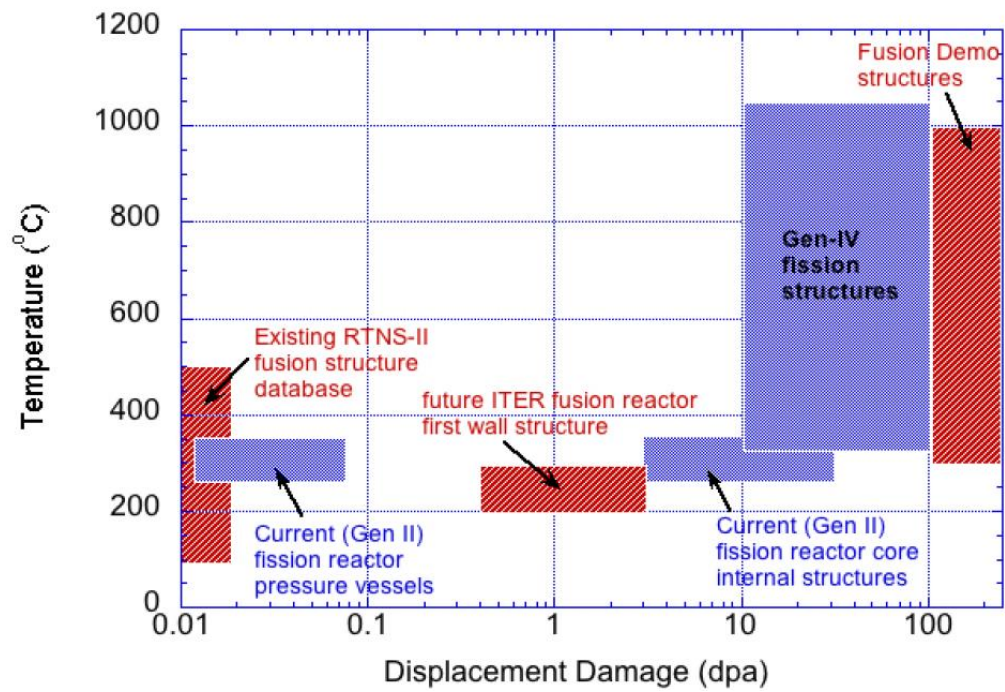
Fig 2. Operating temperature and radiation fluence of traditional reactor and next generation reactor
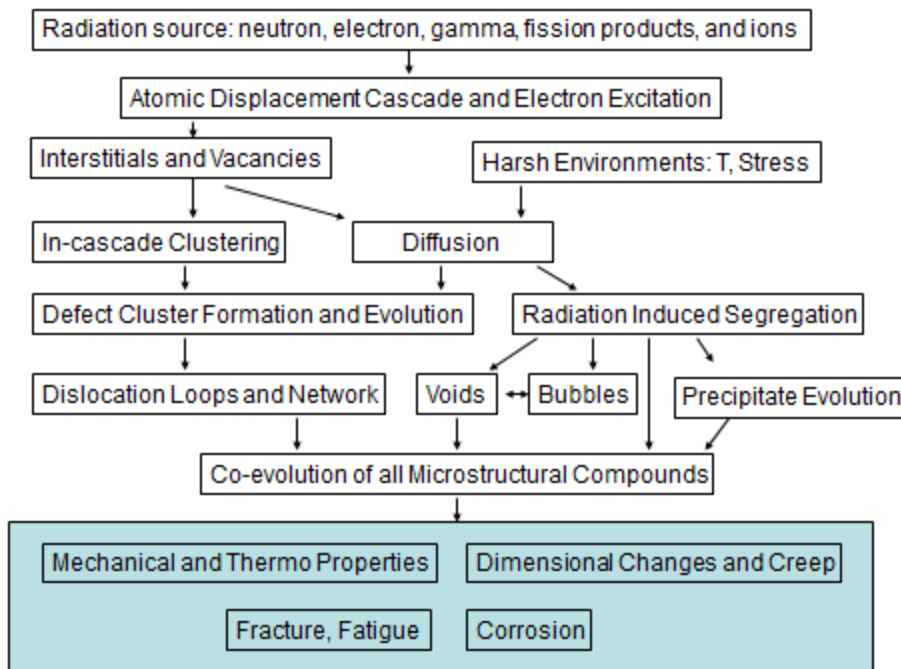
Fig 3. Mechanisms of radiation damage creation

Fig 3. indicates the mechanisms of radiation damage creation. Initially, vacancy clusters and interstitials are formed after interstitials and vacancies are created during an ion damage event. Those vacancy clusters will form voids and bubbles. In contrast, interstitial clusters might lead to dislocation loops and networks. All these microstructural compounds combing with harsh environments would cause serious consequences such as creep, fracture, corrosion etc., structures which can assist interstitial and vacancy recombination can serve to improve radiation tolerance in materials.

Radiation damage creation and evolution in nanograined metals has been a subject of great interest for development of radiation tolerant materials [3,4]. Previous studies have revealed that free surfaces, grain boundaries, and precipitate-matrix interfaces will reduce the number of defects by acting as defect sinks [5-7]. By incorporating these types of structures into materials they can develop self-healing properties leading to higher radiation tolerance [5-8]. However, there has been a challenge to understand the phenomena behind this. Since interstitials typically have a higher mobility than vacancies, damage creation near a grain boundary will lead to quick interstitial diffusion towards the boundary, causing interstitial depletion. Consequently, vacancies within the domain lose interstitial partners for defect recombination. Therefore, quick interstitial diffusion towards the boundary in nanograined materials also means high vacancy accumulation inside the domain [9]. This will have two consequences: at a high temperature with sufficient mobility, vacancies may form voids; at a low temperature vacancy number may continue increasing with increasing dpa values and eventually cause amorphization. In

either case , nanograined metals lose the capability of defect self-repairing. Since the above prediction leads to the opposite of experimental observations, it has been suggested that grain boundaries must be able to emit interstitials back into the domain to recombine with vacancies [9].

Future nuclear reactors will likely require operation at a higher temperature, neutron flux, and pressure. These future reactors and their extreme environments necessitate the need for nano-grain metals that can withstand creep, embrittlement, and swelling. Even though nano-grain metals have to face other challenges such as thermal stability [8,10], gaining atomic understanding between grain-boundaries and defects could prove beneficial. One important report shows that boundaries act not only as interstitial sinks, but also as interstitial sources if the vacancies become supersaturated within the bulk metal [7]. However, the atomic scale details and mechanisms are still unclear. It is still not well understood what mechanisms cause grain-boundaries to attract point defects and emit interstitials.

CHAPTER II

BACKGROUND

2.1 Ion Solid Interactions

When energetic ions go through materials, the interaction between the ion and solid are extremely complex. **Fig** 4. indicates that energy losses are from many aspects, including secondary electrons, sputtered ions, collision with other atoms and electron excitation.

Two energy loss mechanisms are primarily responsible for ion energy loss in a solid: nuclear and electronic collisions .In nuclear collisions, energy loss can be mathematically interpreted by the energy transferred per unit length through elastic collisions. This energy loss rate is defined as the nuclear stopping power. Nuclear collisions transfer energy through elastic columbic interactions and result in atom displacements and increased lattice disorder. Electronic collisions are characterized by the electrons of the target material becoming excited or getting removed from an orbital. Formula 2.1 shows the general form of the total stopping power of an ion in a solid where subscripts n and e symbolize nuclear and electronic collisions, respectively.

$$\frac{dE}{dx} = \frac{dE}{dx}|_n + \frac{dE}{dx}|_e \qquad (2.1)$$

Primary ion

Secondary electrons

e⁻   e⁻

e⁻   e⁻

Sputtered ions

X-ray

Collision cascade
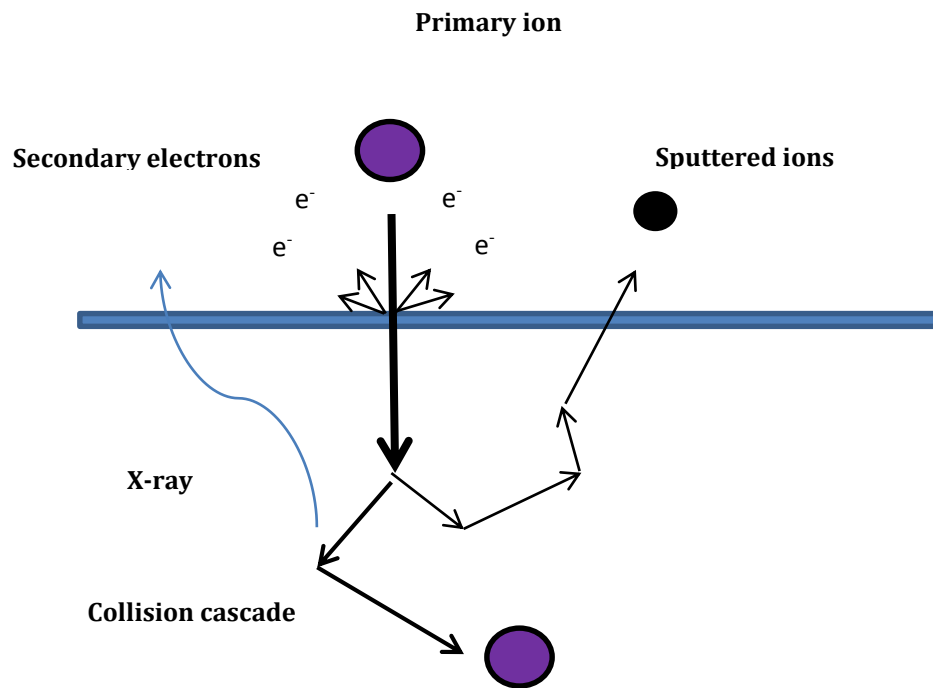
Fig 4. Energy loss mechanism of an incident ion

Fig 5. demonstrates nuclear energy loss and electronic energy loss in different ion energy regimes. Nuclear energy loss dominates when ion velocities υ are lower than the velocity of atomic electrons v_0 (Bohr velocity). At these velocity values, an ion carrying its electrons neutralizes by capturing orbital electrons. Nuclear energy loss decreases as $1/E_0$ with increasing velocity of ions, and electronic energy loss starts to prevail above certain energy. Electronic energy loss is proportional to $E^{1/2}$ in the velocity range from $0.1v_0$ to $Z_1^{2/3}v_0$. In this energy interval, the ion has a variable charge state ranging from neutral at the lowest energy to a bare positive point charge at the highest energy. Once the ion velocity reaches above $Z_1^{2/3}v_0$, the ion can be thought as a positive point charge that possesses velocities exceeding the mean orbital velocities of electrons in target atom.
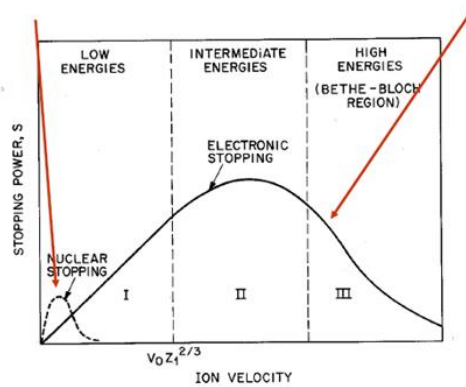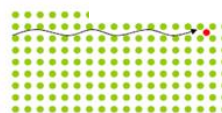
Fig 5. Nuclear energy loss vs. electron energy loss

Understanding radiation damage creation in solids is important for a wide range of applications in the nuclear industry. Upon ion bombardment, nuclear collisions lead to formation of damage cascades. A damage cascade, as seen in **Fig** 6., is a highly disordered region created at the site of a nuclear collision immediately after the incident ion transfers a large amount of energy via columbic interaction to a lattice atom. This lattice atom is known as the primary knock on atom (PKA) and is directly responsible for the creation of the large number of interstitials and vacancies produced in the damage cascade region.
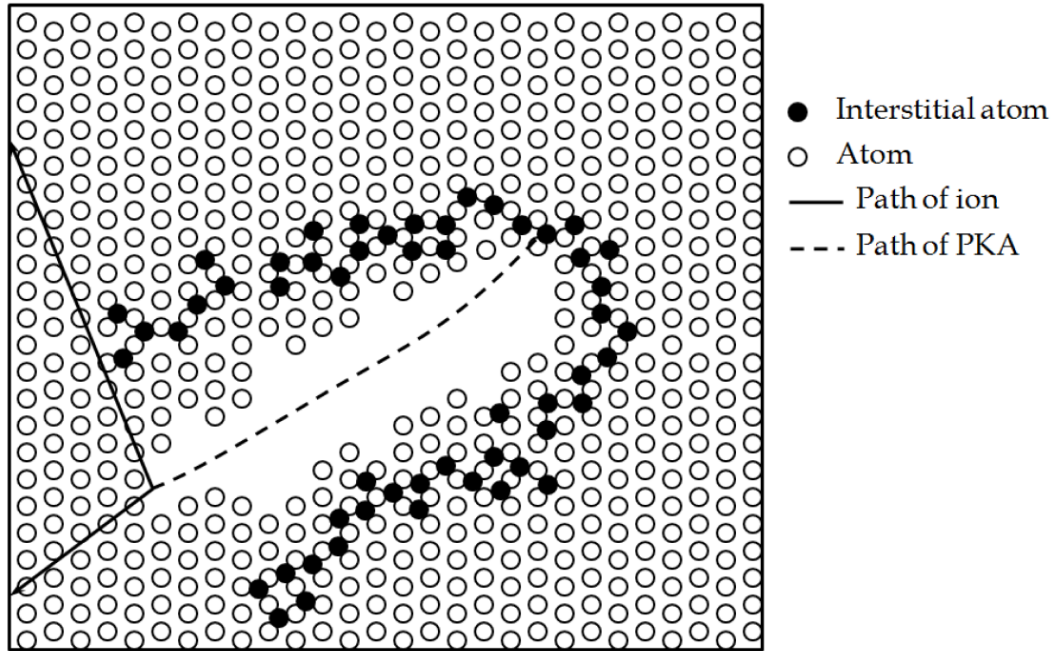
Fig.6. Typical damage cascade

The evolution of damage cascades, as seen in **Fig** 7., can be divided into 4 stages:

1) a collision stage in which lattice atoms are displaced by knock-on and recoiled atoms;

2) a thermal spike stage in which atoms that have enough kinetic energy can take interties

site converting their kinetic energy into potential energy in the form of increased lattice

strain; 3) a quenching stage in which point defects recombine and the defect dense region

begins to dissipate energy through defect migration; 4) an annealing stage in which

structure relaxation and defect clustering occur forming permanent defects. The first three

stages occur at time scales too short for direct experimental observation, so studies on their

atomic scale details have relied heavily on molecular dynamics (MD) simulations.
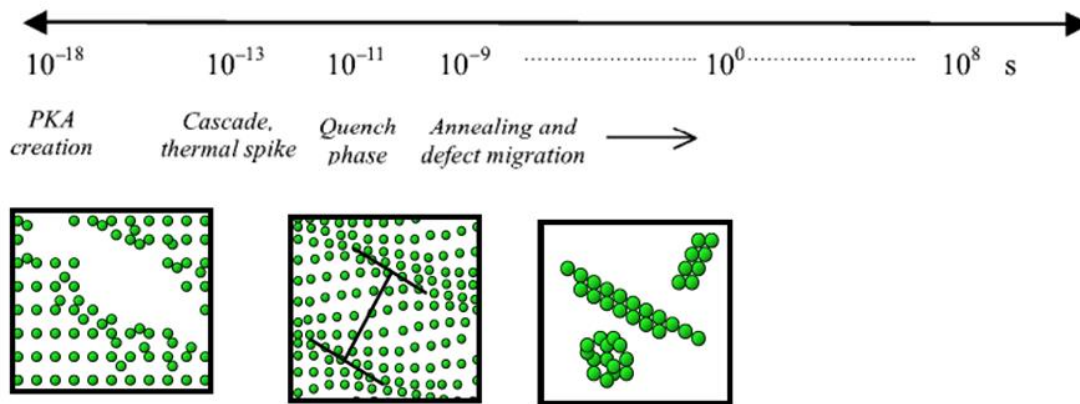
Fig 7. Stages of cascade

2.2 Molecular Dynamics

Molecular dynamics is a computation based simulation method. Based on classical

mechanics, movement of atoms can be predicted if interaction between atoms are well

defined and precisely described. This method was popularized in the 1950s [11,12] when

people began realizing its importance. After decades of improvements, MD simulation

has been wildly used in many areas including material science, engineering, physics, and

chemical engineering, due to improvements of computer power. The foundation of MD

is Newton's second law.

Newton's equation is given by

$$F_i = m_i a_i$$

(2.2)

where F_i is the force exerted on atom i, m_i is the mass of particle i and a_i is the acceleration

of particle i.

Newton's second law can also be expressed as

$$F_i = -\nabla_i V$$

(2.3)

In order to integrate Newton's equation, we can make the assumption that the position

and the velocity of each atom can be approximated by a Taylor series expansion.

$$r(t + \delta t) = r(t) + v(t)\delta t + \frac{1}{2}a(t)\delta t^2 + ...$$

$$v(t + \delta t) = v(t) + a(t)\delta t + \frac{1}{2}b(t)\delta t^2 + ...$$

$$a(t + \delta t) = a(t) + b(t)\delta t + ...$$

(2.4)

Where r is the position, v is the velocity, a is the acceleration.

To derive the **Verlet** algorithm one can write

$$r(t + \delta t) = r(t) + v(t)\delta t + \frac{1}{2}a(t)\delta t^2$$

$$r(t - \delta t) = r(t) - v(t)\delta t + \frac{1}{2}a(t)\delta t^2$$

(2.5)

Summing these two equations, one obtains

$$r(t + \delta t) = 2r(t) - r(t - \delta t) + a(t)\delta t^2$$

(2.6)

The Verlet algorithm uses positions and accelerations at time t and the positions from time t-Δt to calculate new positions at time t+Δt. The Verlet algorithm uses only relative velocities. Two advantages of the Verlet algorithm are, 1) it is straightforward. 2) the storage requirements are modest. The disadvantage is that the algorithm is of moderate precision.

Empirical potentials

The most important, as well as challenging, part of MD simulation is the empirical potential. Because the foundation of MD simulations is classical mechanics, it can't deal with electron behavior, which is based on quantum mechanics interactions. As a result, empirical potentials contain parameters that can be fitted using Ab-initial simulations or experimental results. There are many models that can be used to give these potentials each with varying degrees of accuracy depending on the type of systems.

Pair potential is the simplest model. Formula 2.7 is the expression of the <u>Lennard-Jones potential</u> [13], also known as the 6-12 potential. This potential describes interactions between atoms of simple systems, such as noble gases and some liquids.

$$U(r) = 4\varepsilon \left[\left(\frac{\sigma}{r} \right)^{12} - \left(\frac{\sigma}{r} \right)^{6} \right]$$

(2.7)

In comparison, embedded atom method (EAM) can provide a multi body potential. When dealing with metallic systems, potentials from electrons contribution play an important role, which can't be ignored.

Murray Daw [14.15] and Mike Baskes [16] tried to take into account all neighbor atoms' contribution. Finis improved it by connecting it to tight binding theory. The final form is shown in formula 2.8. This formula, supported by many studies, has been proven to be a good approximation [17-19].

$$E_i = F_\alpha \left(\sum_{i \neq j} \rho_\beta(r_{ij}) \right) + \frac{1}{2} \sum_{i \neq j} \phi_{\alpha\beta}(r_{ij})$$

(2.8)

As used in formula 2.8, r_{ij} is the distance between atoms i and j, $\phi_{\alpha\beta}$ is the pair- potential function, ρ_β is the contribution form electrons and F is an embedding

16

function that represents the energy required to place atom i of type α into the electron cloud.

Ensembles

In MD simulations, ensemble is also a critical factor. The ensemble applied depends on the type of interaction the simulated volume has with the outside environment. There are three ensembles that generally used: microcanonical ensemble (NVE), canonical ensemble (NVT) and isothermal-isobaric ensemble (NPT).

In the microcanonical ensemble (NVE), number of atoms (N), volume (V) and energy (E) don't change with time, so that the total energy is conserved. In the canonical ensemble (NVT), number of atoms (N), volume (V) and temperature (T) are constant. This system is used to simulate the system matching its surrounding temperature, while keeping the shape and volume of the system constant. In the isothermal-isobaric ensemble (NPT), number of atoms (N), pressure (P) and temperature (T) are conserved. The ensemble is useful for creating relax structures initially.

Large-scale Atomic/Molecular Massively Parallel Simulator (LAMMPS)

LAMMPS is one of the most popular software packages for performing MD simulations. Sandia National Laboratories created this program and released it in 2010. [20] Because it's written in C++ and open source code, users of LAMMPS keep making

it more powerful and useful.   Sandia National Laboratories and independent users develop more functions every year for this program.

Input, potential, and structure files are essential parts for using LAMMPS. The input file contains information relating to initial structural relaxation, radiation damage creation and post damage annealing. Potential files hold all information regarding parameters and models used in MD simulations. Contained in the structure file is all information about initial atom positions and velocities. All of these files used for simulations in this study are included in Appendix A.

Nudged elastic band (NEB)

The NEB method is a used to calculate transition path and its' related energy. Replicas are created to form a chain which represents the path from a starting point to an ending point. **Fig** 8. shows the principle of the NEB method. Multiple paths are tried until the path of minimum energy is found. This data is used to find the minimum energy barrier, as seen in **Fig** 8**.** The particular strength of this method lies in its ability to be applied regardless of system temperature.

LAMMPS provides a package, that use NEB to calculate energy barrier. The file for NEB calculation in this study is included in Appendix B.
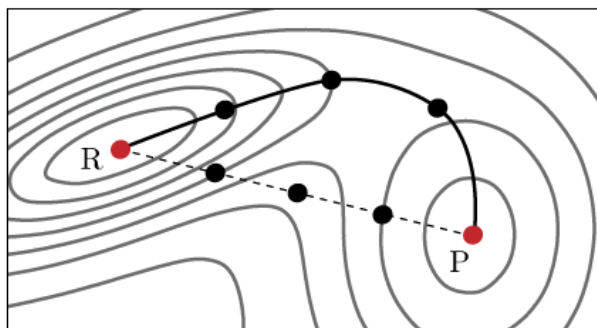
(a)
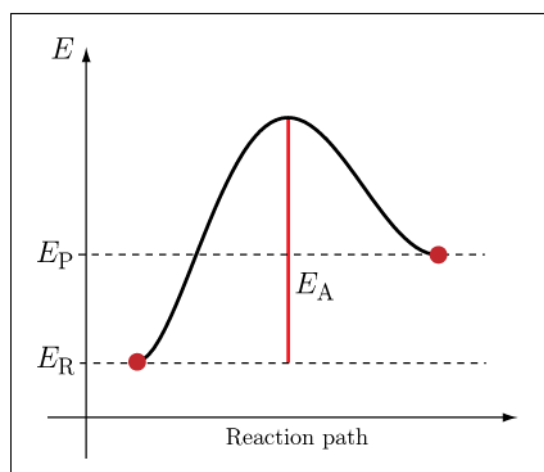
(b)

Fig 8. Sketch of nudged elastic band method.

2.3 Point Defects cnd Their Formation Energy

Point defects are extremely important when studding microstructure changes in materials since they are the precursors to large defect structures such as voids, dislocation loops and SFT. There are two kinds of point defects: vacancies and interstitials. These point defects can be seen in **Fig** 9, highlighted by the black circles. A vacancy is a lattice site missing an atom. An interstitial is an atom found outside of a lattice site. In this studies, C++code was applied to characterize vacancies and interstitials, which is attached in Appendix C.
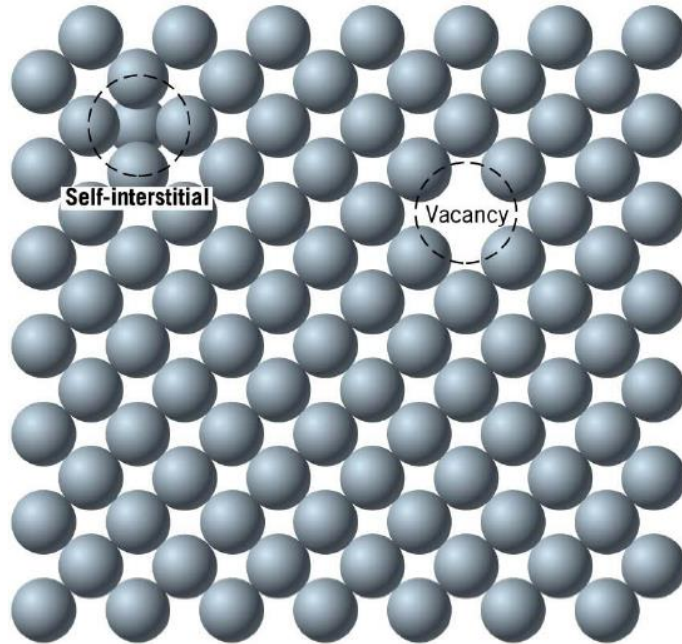
Fig 9. Interstial and Vacancy

To calculate the defect formation energies, the created cell was structurally relaxed through energy minimization. Then an interstitial or a vacancy was introduced in the region of interest and a second energy minimization was performed, to allow the point defect find its stable location. The formation energies of point defects are calculated by

$$E_f^V = E_2 - \frac{N-1}{N} E_1$$

(2.9)

and

$$E_f^I = E_2 - \frac{N+1}{N} E_1$$

(2.10)

where E_1 is potential energy for the whole system, E_2 is potential energy of system with one vacancy or one interstitial, and N is the total atom number in the system.

2.4 Grain Boundary (GB)

When two grains meet together, the interface is known as a grain boundary. GBs are treated as a kind of 2D defect in a crystal. GBs are so common and important, that a well-established theory has already been developed to describe their behavior.

Coincident site lattice (CSL) is the parameter to define GBs by using Σ, which is the reciprocal of the ratio of coincidence sites to the total number of sites. There are also two other parameters used to describe GBs: rotation axis and rotation direction. For

example, (013) [100] Σ = 5 represents a GB that has Σ equal to 5, the rotation axis is 1 0 0 and direction after rotation is 0 1 3.

2.5 Interactions detween Grain Boundaries cnd Irradiation

There are many experimental research works provide evidences that grain boundary structure exhibit abilities to attract defects created from irradiation. **Fig**.10 shows one of examples, Hen and his collaborators found that void-denuded zone (VDZs) are investigated on grain boundary after He irradiation in Cu. (a) indicates the structure of grains in Cu, (b)(c) show ~ 50 nm VDZs after He irradiation[21].
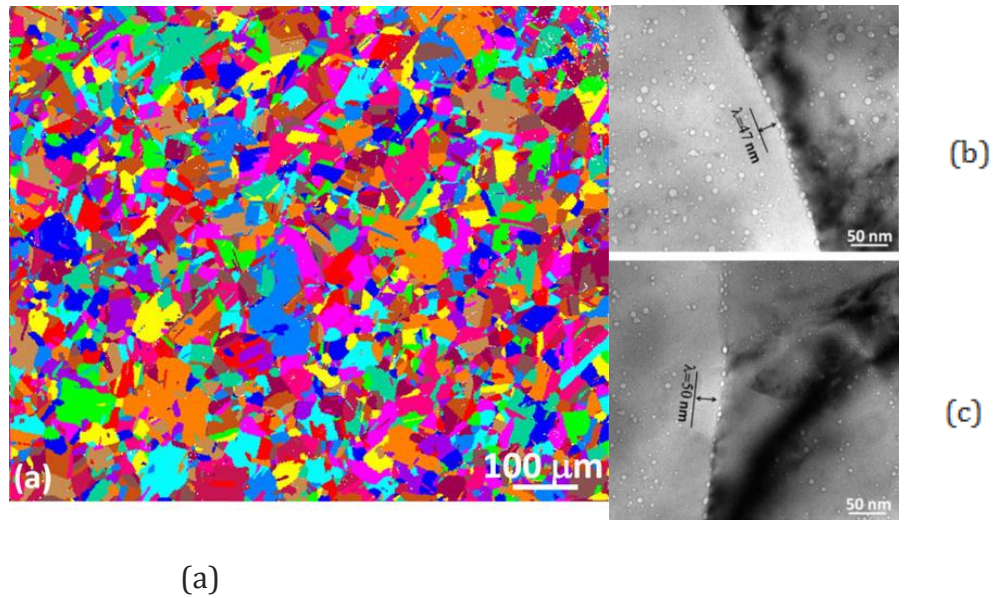
Fig. 10 Radiation-induced damage features at grain-boundaries (a) EBSD (electron back-scatter diffraction)image of high-purity Cu (b) VDZ around a 43° GB; (c) VDZ near a 48° GB [21]

In order to explain what are observed from experiments, people have been tried to use simulation and modeling. There are three questions we need to figure out:

(1) how defects are trapped by a grain boundary

(2) how defect are annihilated at a grain boundary, and

(3) what are upper limits of radiation tolerance of boundary-engineered metals.

CHAPTER III

EXPERIMENT SYSTEM AND SAMPLE INFORMATION

3.1 1.7 MeV Linear Accelerator

3.5 MeV Fe^{2+} irradiations were done at Texas A&M University using a 1.7 MV Linear Accelerator in Dr. Lin Shao's ion beam lab. **Fig** 11. is a schematics of accelerator used to perform the irradiations. To provide the iron ions, an iron cathode was used in a sputtering ion source. This ion source uses a Cs gas to sputter iron atoms from the surface of the cathode, to create negatively charged iron ions. These ions are then accelerated and focused and sent through a low energy bending magnet to filter out all other ion species which came out of the sputtering ion source. After purifying the beam to contain only iron atoms, the negatively charged beam is accelerated in the first stage of the tandem acceleration column.

The negatively charged atoms are pulled toward the high positive voltage at the center of the column, where they pass through a nitrogen stripper canal. In this canal nitrogen gas is present to remove electrons from the iron ions to make the beam positively charged. Since the beam is now positively charged, it is accelerated away from the high positive voltage in the second stage of acceleration. The beam is then passed through a high energy magnet and bent to a specific chamber line. This step is extremely important as this high energy magnet acts as an energy filter, selected a beam of only a specific

energy, and removing the neutralized beam coming out of the stripper canal. This beam is then shaped in the desired manner and sent to the target chamber, to be used for irradiations.

The samples were placed in a 6mm×6mm area using silver paste onto a heated stage over which the beam was defocused to provide a uniform current density. The chamber was then evacuated to a pressure equal to or less than 6×10^{-6} Torr. After acceptable vacuum was reached, the heater rod was used to bring the stage and samples to $475\,^{\circ}\text{C}$. After these conditions reached, the defocused beam was allow to impinge on the surface beginning the irradiation. Beam was run at an average current of 200nA until the fluence reached 1.75×10^{17} ions/com^2, which is equivalent to 200dpa.
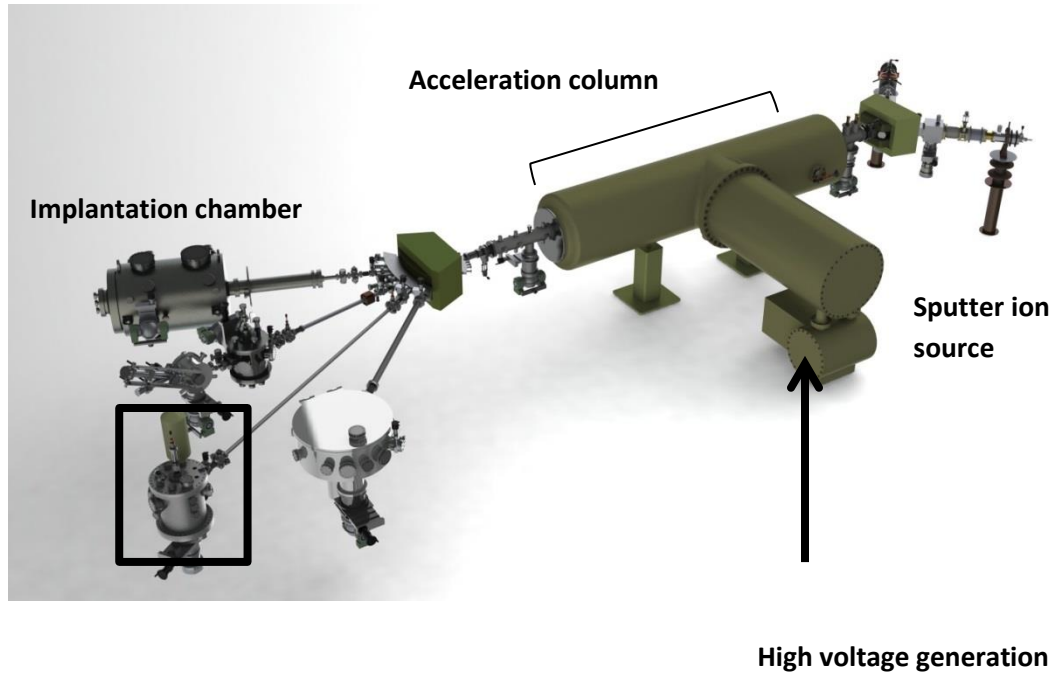
Fig 11. Schematics of accelerator (drawn by Lloyd Price)

3.2 Equal Channel Angular Extrusion (ECAE)

Equal channel angular extrusion (ECAE) is a technique used to refine meals and alloys in order to change their microstructure. Lots of deformation and strain are added during the ECAE process. To perform this process, a bar of metal is forced through a channel with a 90 degree angle repeatedly until the desired grain size is obtained (as seen in **Fig** 12) [22]. The ultra-fine grain ECAE processed samples used in this study were provided by Dr. Hartwig.
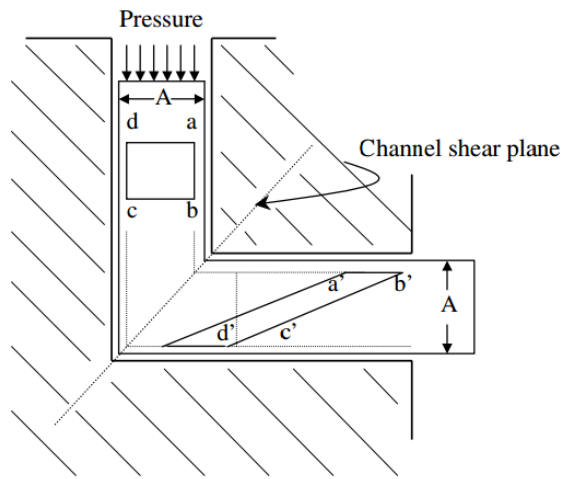
Fig 12. Schematic illustration of the ECAE process [22]

CHAPTER IV

ATOMIC UNDERSTANDING OF DEFECT ANNIHILATION AT GRAIN

BOUNDARIES IN ALPHA-FE[*]

4.1 Background

In fission reactors where stainless steels are widely used as in-core structural

components, materials are exposed to high fluence neutrons with accumulated radiation

damage up to a few hundred displacements per atom (DPA) [23,24]. High energy fission

product particles resulting from neutron-solid interactions create collision cascades.

Majority of interstitials and vacancies in the cascades can quickly recombine within a

fraction of one picosecond, but those point defects escaping the dynamic annealing

process develop into extended defects such as dislocations, stacking fault tetrahedra and

voids [8,10,25-27]. The radiation-induced microstructure and microchemistry changes

eventually lead to various structural failures including swelling, hardening, embrittlement,

stress corrosion cracking, and creep[4,24,28]. Towards development of radiation tolerant

materials with self-repairing capabilities, previous studies have shown that free surfaces,

grain boundaries, and precipitate-matrix interfaces can act as defect sinks to trap and

recombine defects [29-31]. Among various structure-engineered materials, nanograined

or nanolayered metals have been a subject of great interest [5-7,32]. Although thermal

stability of nanograins, i.e. grain coarsening upon annealing, presents a challenge for

practical usage, grain stabilizations have been achieved through introducing additives or

by fine tuning of plastic deformation conditions[33-34]. Most recently, nanocrystalline metals having exceptional thermal stability have been reported with the design guided by a new thermodynamic model[35]. These findings show great promises for applications of grained-engineered metals in reactors. Further materials developments require atomic scale details, often beyond direct experimental observations. One complexity of the boundary effect is found in recent modeling studies, which show that boundaries act as not only interstitial sinks but also interstitial sources if the vacancies become supersaturated within the bulk[31]. However, many fundamental mechanisms, i.e. atomic scale details of defect annihilation on grain boundaries, remain unknown.

Using single-phase bcc Fe as the model material, we shed light onto atomic scale details of boundary defect sink and annihilation through molecular dynamics (MD) simulations. One key finding is that boundary-defect interactions are not realized by movements of individual defects which keep their identities through the whole processes. Instead, a chain-like group defect is always involved. The study identified two kinds of chain defects, both consisting of alternately positioned interstitials and vacancies. One is denoted as "bulk chain-like" (BC) defect, and the other is denoted as "grain boundary chain-like" (GBC) defect. A point defect can induce BC or GBC defects and, through localized recombination of neighboring interstitial-vacancy pairs along the chain, realizes an equivalent transport from one end of the chain to the other end. BC or GBC defects can

also be induced between a well-separated interstitial-vacancy pair to realize defect annihilation. The present study identifies three defect removal processes and for all of them, BC and GBC defects are both relevant to the patterns of the defect formation energy minima on the boundary.

4.2 Iron Irradiation qn Single Iron cnd Ultra-Fine Iron

3.5 Mev Fe^{2+} was used to irradiate both single crystal iron and ultra-fine grained iron at 475°C to a damage level of 200 DPA. A FIB was then used to make TEM samples to characterize the materials' structural change after irradiation. **Fig** 13. Shows TEM images of single crystal (**Fig**.13 (a)) and ECAE (**Fig**.13(b)) iron after this irradiation. In single crystal iron there are a great number of voids whose size ranges from a few nm to hundreds of μm. In comparison, there is no evidence of voids in the ECAE iron sample. Even at a higher magnification (**Fig** 13. (c)), there still no voids in the ECAE iron sample. These observed differences in void production prove that GB structures are capable of suppressing voids creating during irradiation.
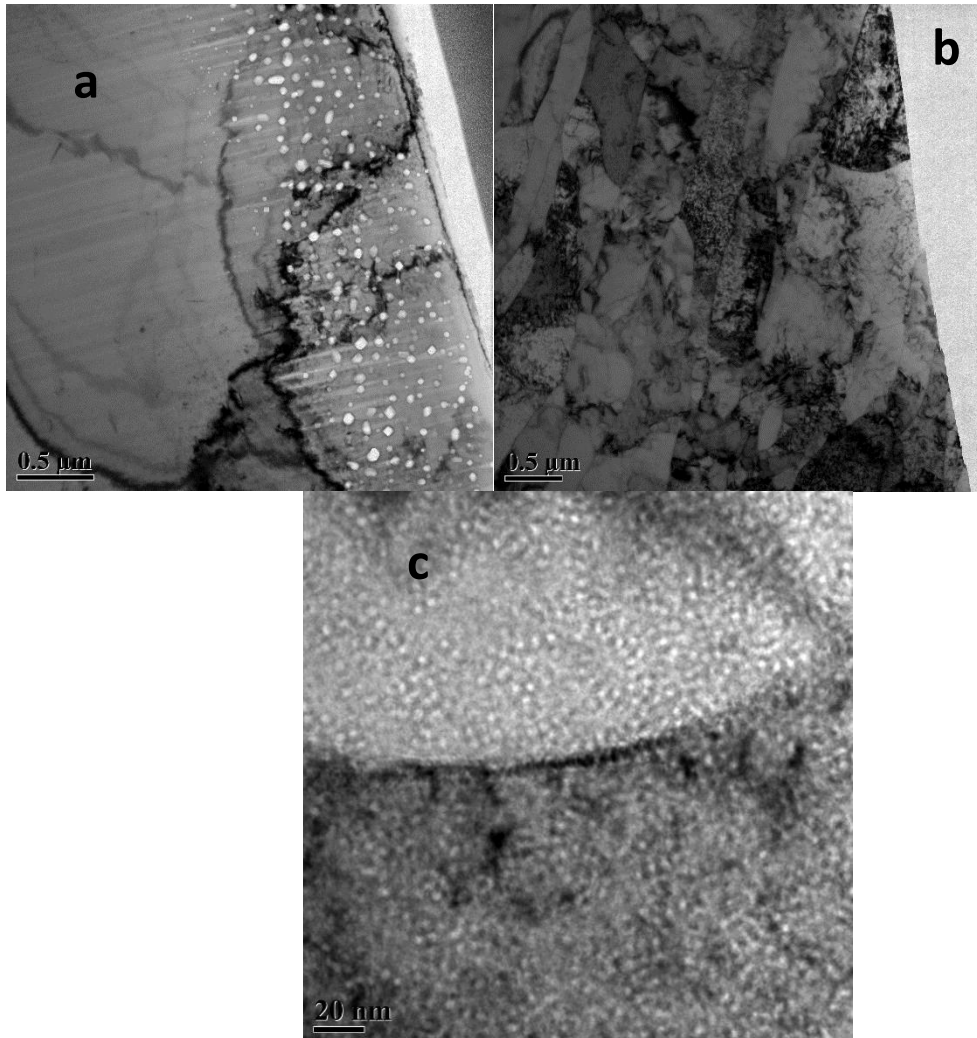
Fig 13. Microstructure of single crystal iron (a) and ECAE pressed iron (b) after 200 dpa 3.5 Mev Fe^{2+} irradiation at 475°C (c) high magnification image of ECAE pressed iron

4.3 MD Simulation qf Radiation Damage kn Iron y ith cnd y ithout GB

The MD simulations of GB structure started with a Fe unit cell containing a $(013)[100]\Sigma = 5$ symmetric-tilt grain boundary created with a tilt angle of 36.8°, as seen in **Fig** 14. The atomic coordinates for the symmetric tilt grain boundary structures were

31

generated using GB studio[36]. The Fe unit cell contains about 70000 atoms, and periodical boundary conditions are applied for cell surfaces. Fig 18. shows the structure of structure of $(013)[100]\Sigma = 5$ symmetric-tilt grain boundary, which are built for next step MD simulation.

36.8°
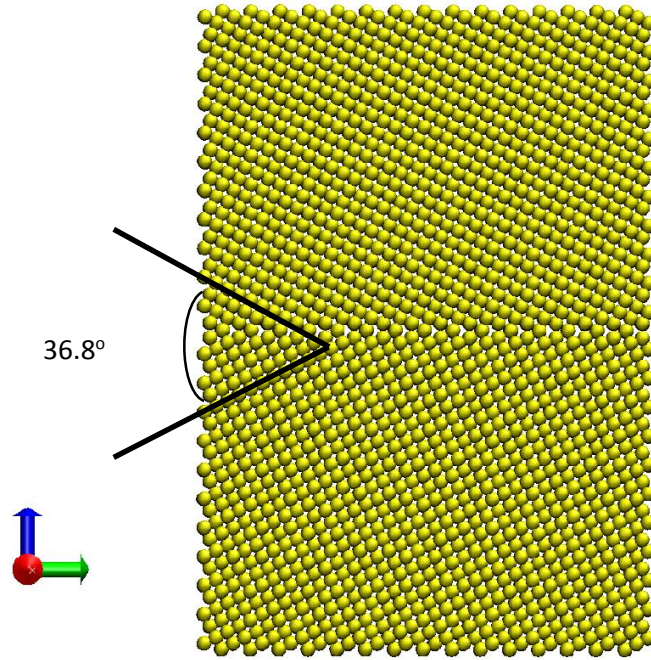
Fig 14. Structure of $(013)[100]\Sigma = 5$ symmetric-tilt grain boundary

The MD simulations are performed by using LAMMPS (Large-scale Atomic Molecular Massively Parallel Simulator) code [9], with Fe potential developed through embedded atom method (EAM) [37]. The EAM potential smoothly changes to Ziegler-Biersack-Littmark potential at short interatomic separation [38]. The cell has a

dimension of 14nm×14nm×14nm, which contains about 250000 atoms. Periodical

boundary conditions are applied. The damage cascade is created by bombardment with

one 3 keV Fe atom, which is incident at 9 degrees away from the cell normal direction.

This avoids ion channeling and helps to confine the damage cascade within the cell. The

cell further contains a grain boundary, which is created by putting two bcc-Fe domains

together. Prior to the ion bombardment, the bcc alpha-Fe is structurally relaxed to

achieve energy minimization. Simulation is performed with the cell temperature at

450K.
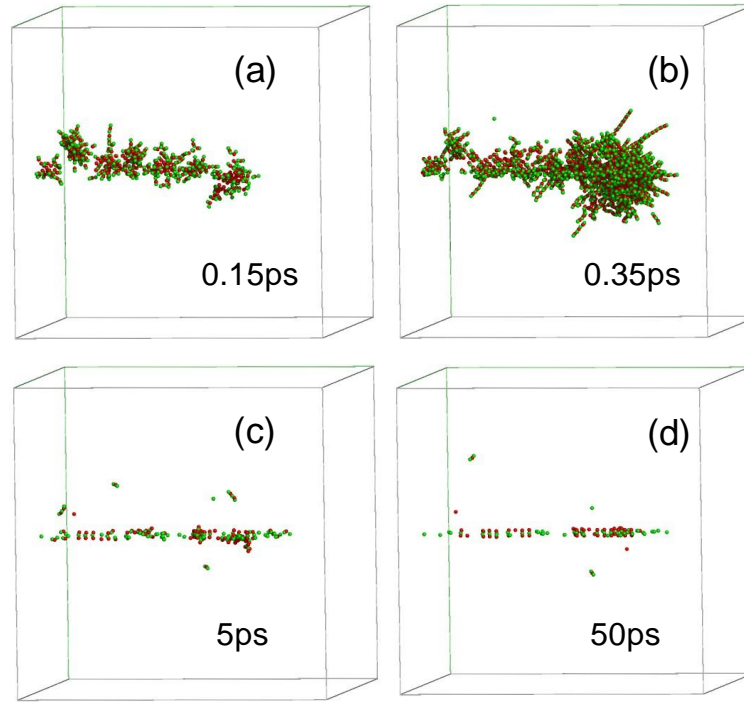
Fig 15. Snapshots of MD simulations of damage cascade evolution upon 3 keV Fe bombardment of alpha-Fe. The cell contains a $(0 - 1\ 3)[100]\Sigma = 5$ grain boundary in the middle.

Fig 15. shows the snapshots of MD simulations at different times after ion bombardment. The blue color refers to interstitials and the red color refers to vacancies. A displaced atom is defined to be an interstitial if its displacement from the closest lattice site is larger than one third of the nearest atomic distance. At a time of 0.35ps, a full damage cascade is developed. The cascade is featured with high density defects along the ion track and rod-like defects "radiated" from the cascade core. These rod-like defects are the so called crowdion defects, which have been previously reported [39,40].

A crowdion defect consists of alternately positioned interstitials and vacancies, created by the successive displacing atoms from one atomic row. The pushing will displace one atom from its lattice site and this newly displaced atom will subsequently displace the next atom from its lattice site. Each successive displacement creates a vacancy. Previous studies have shown that crowdion defects occur only along the direction having the highest linear atomic density [40]. Such crowdion defect formation contributes to a second peak in defect population changes as a function of time [40]. Through recombination between neighboring interstitials and vacancies, a crowdion defect will disappear, with a dumbbell defect or a point defect created at its end.

At the time of 5ps, as shown in Fig. 15, majority of defects in the bulk/domain are annihilated, and many defects appear at the grain boundary. These boundary defects include both interstitials and vacancies. At the time of 50ps, both bulk defects and boundary defects still present but their populations are greatly reduced. The bulk defects are either single vacancies or dumbbell defects, instead of large defect clusters such as stacking faults. These observations clearly show that grain boundaries can act as effective defect trapping sites and defect recombination sites.
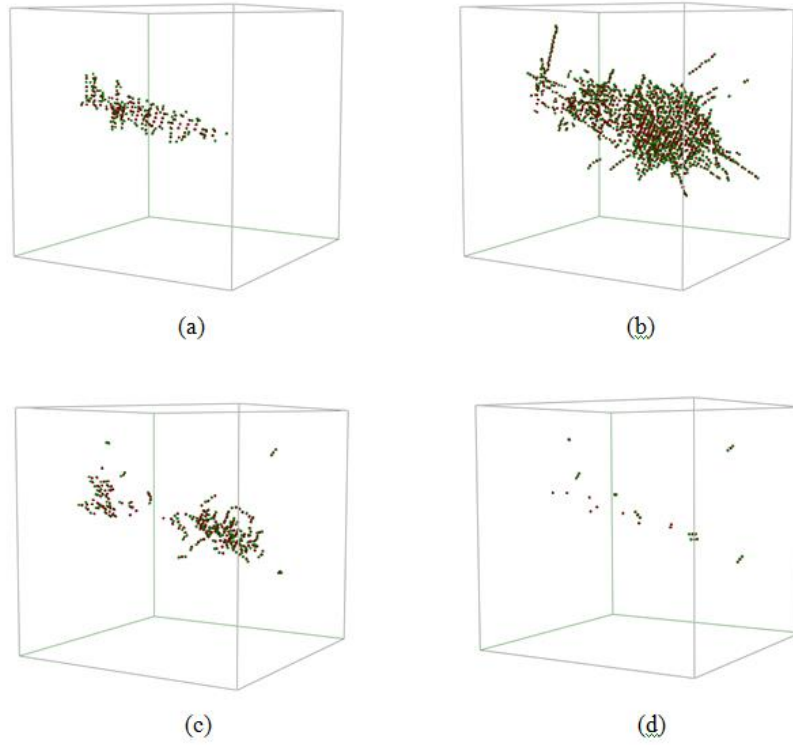
Fig 16. Damage cascade evolution from MD simulation of a alpha Fe crystal irradiated by one 3 keV Fe ion at 0.1 ps,0.3 ps, 1 ps and 30 ps [40]

In comparison, **Fig** 16 shows damage cascade evolution at 0.1 ps, 0.3 ps, 1 ps, and 30 ps after ion bombardment. For best imaging, the cell size is much smaller than the super cell used in MD simulation. The red circles refer to vacancies and the green circles refer to interstitials. From 0.1 ps to 0.3 ps, damage cascade volume is increasing. Also at 0.3 ps, chain-like crowdion defects form with a length ranging from 2 nm to 5 nm. The crowdion defect formation is realized by a series of substituting collisions, with typical knock-on energy close to 30 eV (Fe displacement energy). At 1 ps, significant defect recombination leads to shrinkage of the damage cascade volume. Defect recombination also restores

displacements along crowdions, but leave dumbbell defects at the end of crowdions. One dumbbell defect is featured by two interstitials sitting at each side of an empty lattice site. MD simulations show that the two interstitials are oriented along original crowdion direction. At 30 ps, most defects disappear. It is worthy to note that at this time scale dumbbell defects resulting from crowdion formation represent a considerable fraction of surviving defects.

4.4 MD Simulation of Interaction between Point Defect and Grain Boundary

To model dynamic defect-boundary interactions, one interstitial and one vacancy were positioned at each side of boundary to avoid their annihilation, which is described in **Fig** 17. The defect-loaded cell was then relaxed through energy minimization. As a consequence of the energy minimization, introduced interstitial forms a dumbbell defect by displacing one lattice atom and forming an interstitial-vacancy-interstitial defect complex. At 450 K, simulations started under canonical (NVT) ensemble with moles (N), volume (V) and temperature (T) conserved. The selection of 450 K is able to obtain sufficient defect mobility. The starting of the step performing NVT corresponds to time t = 0 ps, as seen in **Fig** 17. To avoid interference with thermal vibration, a vacancy is defined to exist when an empty lattice site has no atoms found in the radius of one third of lattice parameter (0.287 nm). The same radius is used to define interstitials if their displacements from the nearest lattice sites are larger than this value. The criterion is sensitive enough since the modeling can identify a dumbbell configuration. On the other

hand, the radius is larger enough to avoid overestimation of defect numbers under thermal vibration. Further reducing the radius will increase statistic fluctuations of defect numbers but will not change the conclusion on chain like defect formation and its transport mechanism.
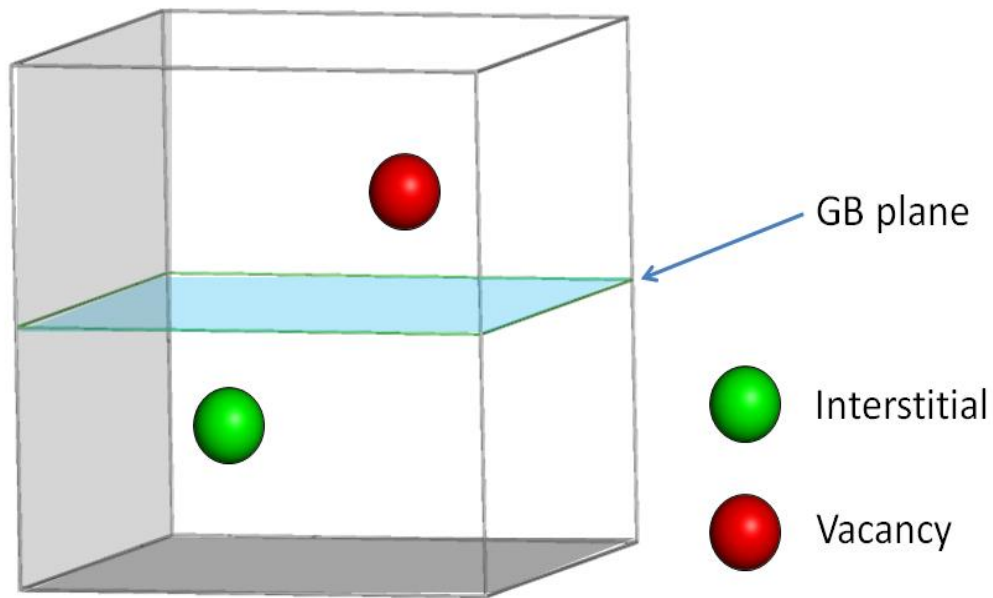
Fig 17.Position of intestinal and vacancy assigned in two sides of GB
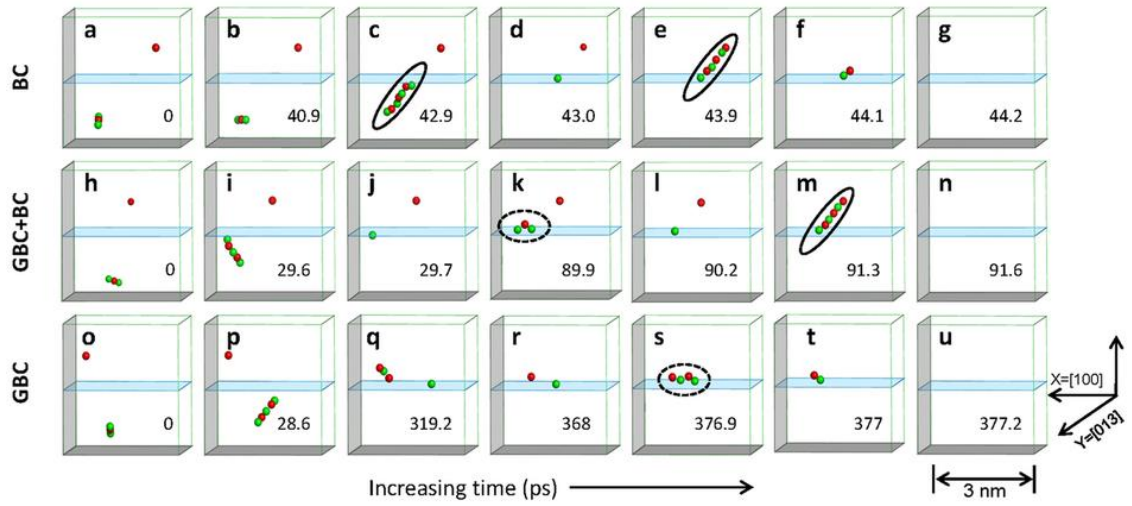
Fig 18. Representative snapshots of a MD simulation of three different defect annihilation processes for (013)[100]Σ = 5 symmetric title grain boundary.

In the beginning the modeling intentionally introduced one vacancy on one side of the grain boundary and one interstitial on the other side. The interstitial quickly changes into a dumbbell defect (a stable small defect complex having one vacancy sitting between interstitials). **Fig** 18. shows three modeling identified defect annihilation processes.
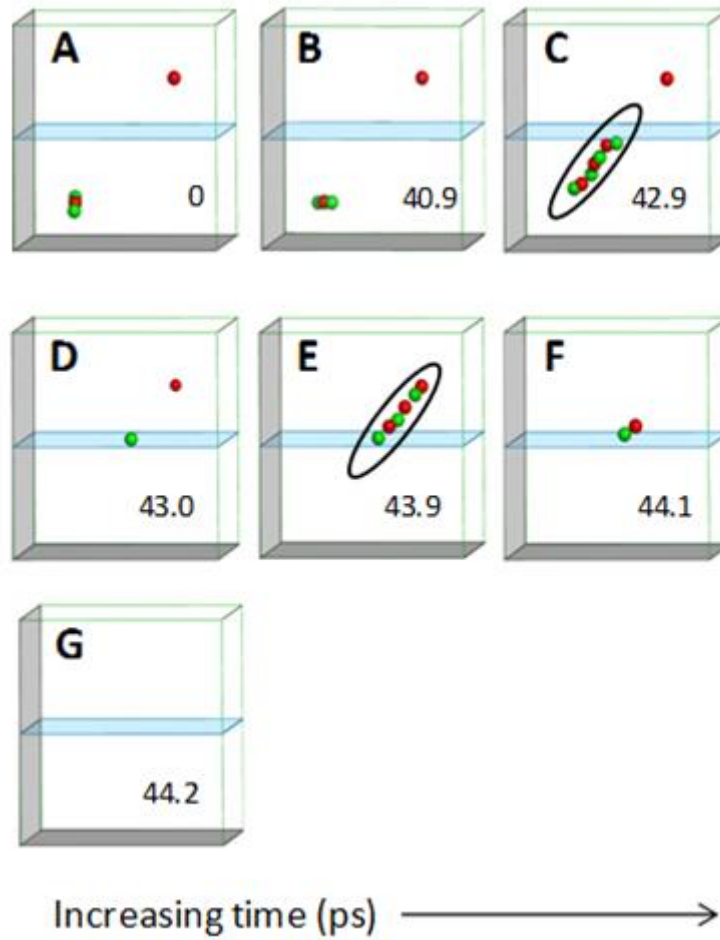
Fig 18-1. Case#1- BC model

In case #1 denoted as "BC model" in the figure (**Fig** 18-1.), a dumbbell defect in the bulk rotates (**Fig** 18-1 b.) and induces a BC defect (**Fig** 18-1 c.). Through subsequent defect annihilation between neighboring interstitials and vacancies on the chain, the inducing defect disappears and leaves one interstitial on the boundary (**Fig** 18-1 d), which

is equivalent to transporting the bulk interstitial to the boundary. Next, with presence of an isolated vacancy in the bulk, the interstitial loaded on the boundary induces another BC defect between the two defects (**Fig** 18-1 e), which eventually leads to complete defect annihilation. One BC defect can be treated as a chain of linked interstitial-vacancy pairs. Different from previously reported crowdion defect, which is a chain of displaced atoms aligned along one crystal axis direction and is often observed around a damage cascade when the inducing defect has sufficiently high kinetic energy[38.39], a BC defect is induced by atoms at thermal vibration energies and is not formed by kinetically displacing the neighboring lattice atoms one after the other in a subsequent manner. Instead, the interstitial-vacancy pairs on the BC defect appear without time orders. Some BC fragments are found to form first at a distance away from the inducing defect, then these fragments connect and complete the chain formation. This means that a BC defect is induced by the stress fields between two ending locations. Our modeling shows that the landing of the BC defect on the boundary always correspond to the sites having the lowest defect formation energies, which appear as periodical patterns on the boundary with the site density determined by the boundary configuration (to be discussed in the present study). This finding reveals the governing factor to determine the capability to transport a defect to the boundary.
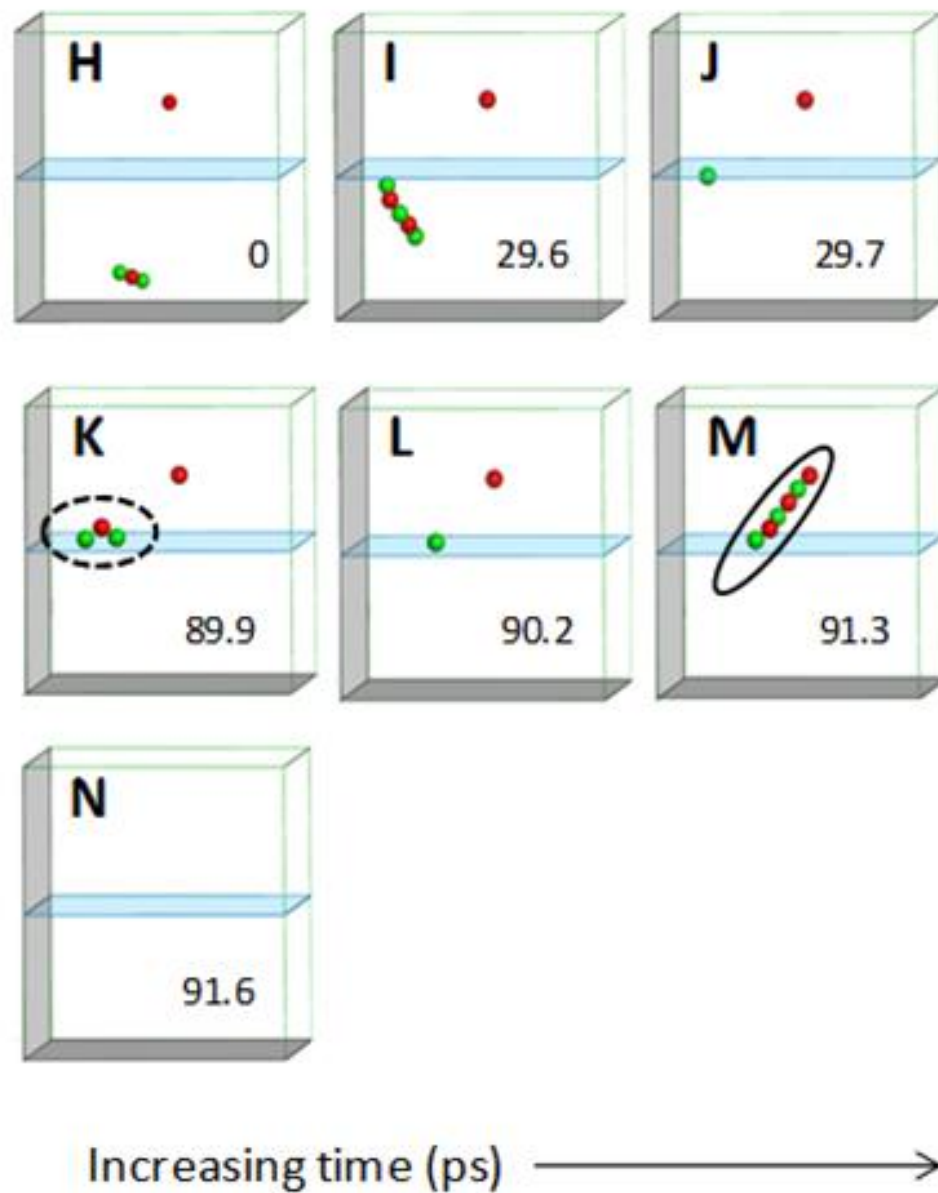
Fig 18-2 Case#2-GBC+BC model

Since a BC defect is induced by stress fields between chain's starting and ending

sites, defect removal through BC model may not occur if two ends are separated too far

away. In a more general situation, described as shown in **Fig** 18-2 and denoted as "GBC + BC model" in **Fig** 18-2 h to n , a boundary-loaded interstitial migrates first on the boundary (**Fig** 18-2 k), then induce a BC defect (**Fig** 18-2 m) to recombine with a bulk vacancy.

Increasing time (ps) ⟶
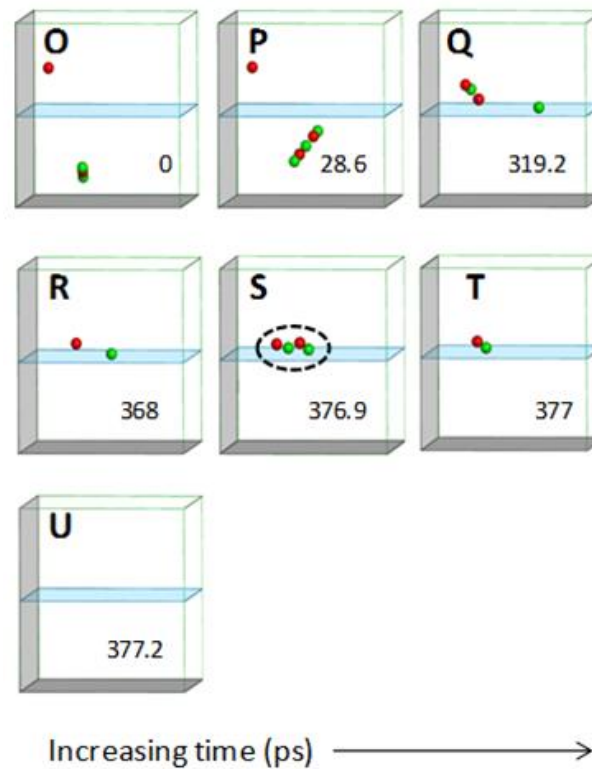
Fig 18-3 Case#3-GBC model

The case #3, denoted as "GBC model" ,as seen in **Fig** 18-3, o to h, is a defect annihilation mechanism involving the step of trapping one interstitial and one vacancy on the boundary but the defect pair is separated over a distance more than one lattice spacing

(**Fig** 18-3, o to r). Although vacancy is less mobile, it still can "transport" to the boundary

through BC defect formation (**Fig** 18-3 q). Induced by stress fields between the defect pair,

each defect migrates on the boundary through GBC defect formations. Eventually, one

GBC defect links the two defects and realizes defect removal (**Fig** 18-3s).

(a)   (b)
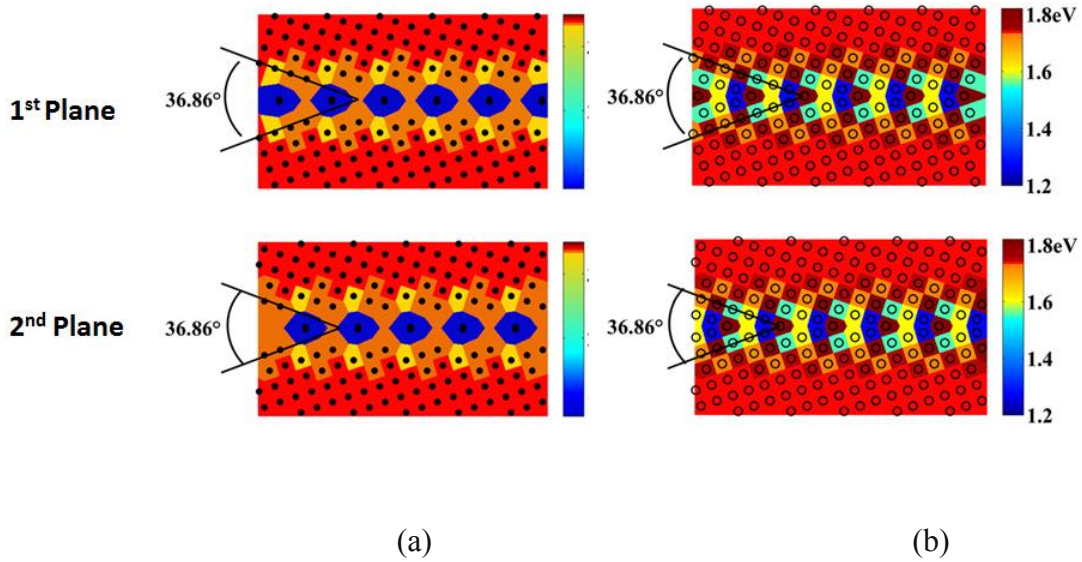
Fig 19. Formation energy of interstitials (a) and vacancies (b) in the bulk and at the boundaries of $(013)[100]\Sigma = 5$ symmetric-tilt grain boundary

To show the dependence of E_{min}^V and E_{min}^I patterns on boundary

configurations, **Fig** 19. plots the energy mapping of E_f^V and E_f^I over symmetric tilt grain

boundaries $\theta = 36.86°$ for $(013)[100]\Sigma = 5$.

The energy scale bar is provided. The hollow circles refer to vacancies and the

solid circles to interstitials. These interstitials sites are not octahedral and tetrahedral

interstitials since both are not energetically favorable. For interstitials in the bulk, energy minimization favors dumbbell defect formation around one lattice location. Close to the boundary, isolated interstitials become energetically favorable to form and corresponding stable locations are identified by allowing structural relaxations in simulations.

Each E_{min}^I and E_{min}^V region contains, usually, multiple sites for interstitials or vacancies to occupy, which leads to zigzag like configurations of GBC defect. A GBC defect can form on the same plane (The 1st or 2nd planes denoted in **Fig** 20.)
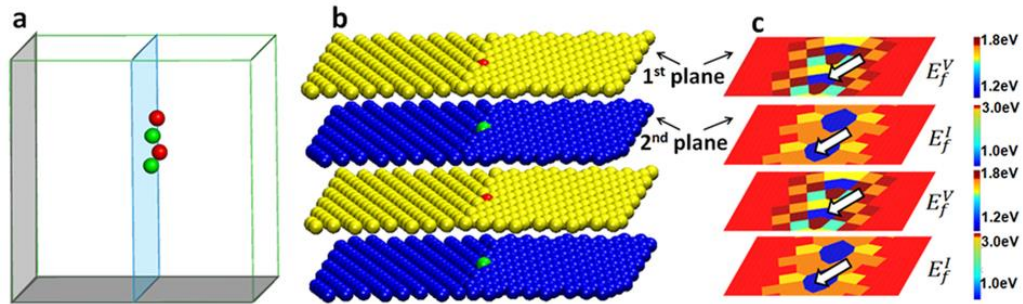
Fig 20. Comparisons of (a) MD simulation observed GBC defect and (b) schematics of lattice locations of defects in the GBC defect and (c) corresponding E_{min}^I / E_{min}^V sites for (013)[100]$\Sigma = 5$ symmetric tilt grain boundary.

A GBC defect has specific configurations: its interstitial corresponds to the boundary site of the lowest interstitial formation energy E_{min}^{I} and its vacancy corresponds to that of lowest vacancy formation energy E_{min}^{V}. MD simulation shows that a GBC defect is formed by displacing a lattice atom from E_{min}^{V} site to the immediate neighboring E_{min}^{I} site. **Fig** 20. shows the correspondence between a GBC defect and defect formation energy on the boundary. The arrows mark the allowable sites for interstitial and vacancy formation as predicted by formation energy minima, which agree with GBC defect configurations. The GBC defect, shown in **Fig** 20.(a), was obtained from modeling (**Fig** 18-3 s.). When bonding two bcc crystals to form a symmetric grain boundary, joining regions of the 1st planes and the 2nd planes have different atomic interactions, where the 1st plane refer to the top surface plane of a bcc unit cell, and the 2nd plane refers to the middle plane, consisting of the center atoms of the unit cell. Interstitials and vacancies in the GBC defect are alternately positioned and each defect takes only one site on each plane (**Fig** 20.(b)). The white arrows in **Fig** 20.(c) point to sites occupied by the defects, over two dimensional mapping of vacancy formation energy (E_{f}^{V}) and interstitial formation energy (E_{f}^{I}). Obviously, the defect location correspond to E_{min}^{V} and E_{min}^{I}, i.e. the vacancy in a GBC defect takes one E_{min}^{V} site and the interstitial takes one neighboring E_{min}^{I} on the next plane. The E_{min}^{I} site corresponds to boundary open volume, where the surrounding atoms have inward relaxation and the region is energetically favorable to insert an interstitial type defect. The E_{min}^{V} region are caused by

close vicinity of two meeting atoms and their repulsive interactions lead to outward

relaxation of surrounding atoms which favors vacancy formation.

(a)   (b)
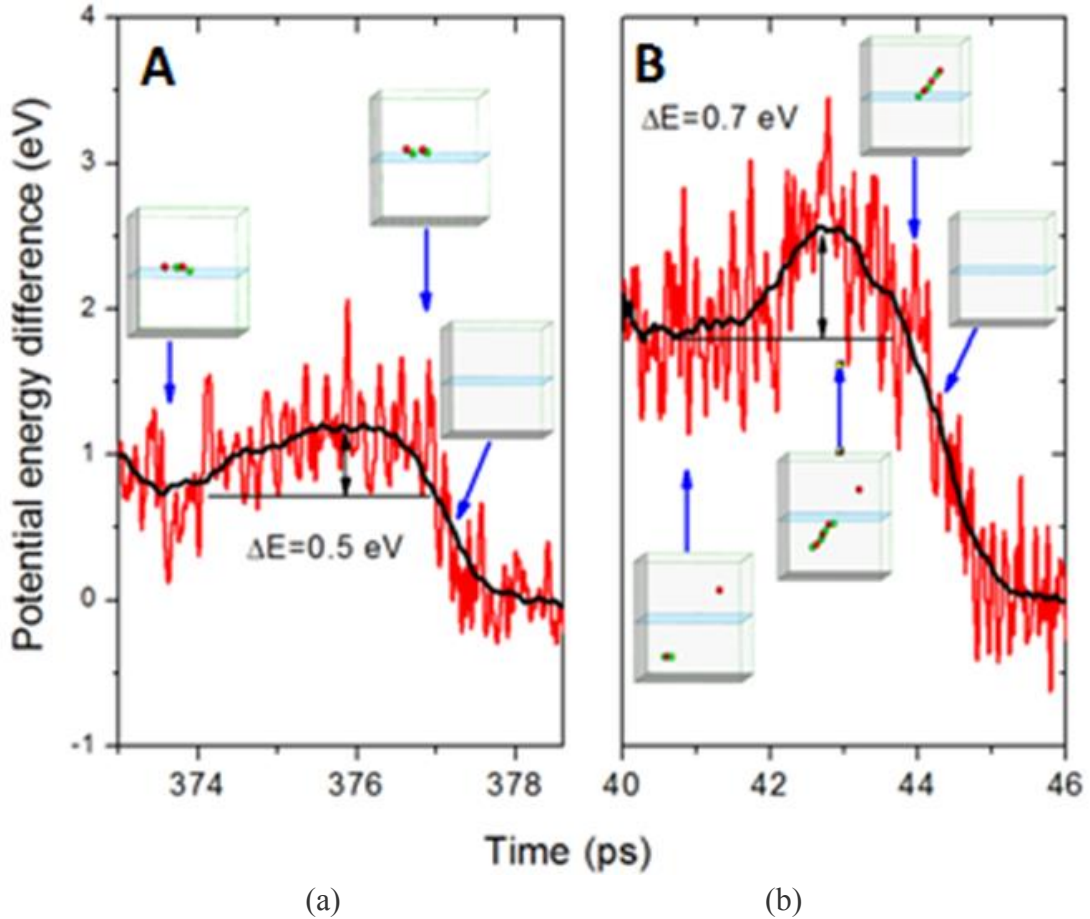
**Fig** 21. The potential change covering the steps of formation and annihilation of a GBC defect

The BC and GBC mediated defect removal processes have relatively small energy

barrier, which can be analyzed from time changes of total potential energy of the selected

volume containing reacting defects. **Fig** 21. plots the potential change covering the steps

of formation and annihilation of a GBC defect (**Fig** 21.(a)) Time dependent potential changes of a localized volume involving the step of forming a GBC defect between a boundary-trapped, well-separated interstitial-vacancy pair and the step of its annihilation, and of a BC defect (**Fig** 21.(b)) the potential changes of the volume involving the successive steps of forming a BC defect to transport an interstitial to the boundary and subsequent forming another BC defect to annihilate a bulk vacancy. The potential energy changes have fluctuations resulting from thermal vibrations and also attempted interstitial-vacancy pair formation/rotation. The energy difference judged by the averaged values between starting step and the energy maximum suggest energy barriers of ~0.5 eV for GBC defect and ~0.7 eV for BC defect. For GBC mediated defect removal, several successive steps, i.e. forming the first BC and then the second BC, occur vary fast and individual energy barrier for each step cannot be differentiated. Overall, the energy barriers are much less in comparison with the energy required to form a crowdion defect, which requires a minimum energy of 6.3 eV, even for the most favorable direction of [111], according to our MD simulations. Our study further suggests that similar GBC defect formation and annihilation mechanisms would apply to dislocations. For an isolated interstitial dislocation in bulk, the edge of the inserted atomic plane expects to have similar atomic scale zigzag roughness. For a given atom on the edge, paired compressive and tensile strain regions are created on each side of the atom. These paired stress fields are zigzag like along the dislocation line. Consequently, GBC like defect chains are allowed to create along the dislocation lines, to assist defect migration and recombination. In fact,

for boundaries of ultra-small angle misalignment, they essentially relax into periodically separated dislocations.

(a)   (b)   (c)
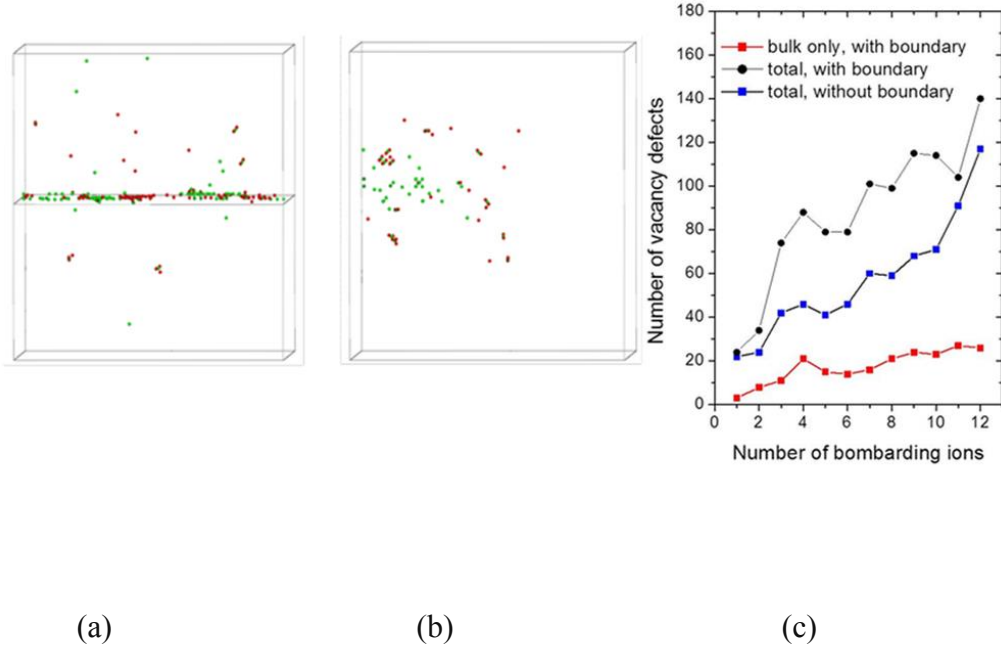
Fig 22. Numbers of vacancy defects left after repeated ion bombardments with or without a grain boundary presented.

In MD simulations of repeating ion bombardments, a 3 keV Fe ion continuously hits the cell at an incident angle of 9° to avoid channeling ion irradiation. The damage cascade is roughly 0.5 nm away from the grain boundary. The time period between two successive ion bombardments is 100 ps. For irradiation in bulk Fe without grain boundary, this time period is much longer than the time required, typically a few picoseconds, to

finish energy/heat dissipation and to form saturated defect population with stable defect clusters formed. For each ion bombardment, microcanonical ensemble (NVE, with the system isolated without heat exchange) was applied for the first 45 ps, followed by NVT for the rest of 55 ps, prior to introducing the next bombarding ion. This is necessary to avoid beam heating from energy contributed by the bombarding ions.

Considering ultra-high dpa encountered by reactor structural components, the stability of boundaries and preservability of boundary effects under extreme radiation conditions need to be evaluated. **Fig** 22 (c). compares the number of residual defects left in the system by repeating ion bombardments of 3 keV in the bulk, with or without the presence of a boundary in close vicinity. Between two successive ion bombardments, structural relaxation is allowed to model interactions among the newly introduced defects and defects left in the previous damage cascades. The damage-overlapping region promotes the formation of large defects due to intense defect interactions. The immobile defect clusters reduce the overall defect mobilities, thus reducing dynamic interstitial-vacancy recombination, and nonlinear damage buildups are expected. For the bulk containing a grain boundary, the boundary effect can be saturated or disappear at high damage levels, if one of the following occurs (1) the boundary defect sink properties favor one particular type of defect (interstitial vs. vacancy) and creates large defect imbalance on the boundary which makes defect recombination difficult; (2) boundary loses its sink properties due to mixing; (3) boundary loses its annihilation property beyond certain limits. Our simulations show that the boundary still has high efficiency in defect removal under

repeated ion bombardments. As shown in **Fig** 22 (c), for a cell containing a grain boundary, the numbers of residual defects (red) in bulk are systematically lower than that without a boundary (blue). However, if not excluding boundary defects, the numbers of total defects (black) are higher than that without a boundary. This can be explained by observation that a boundary vacancy, in addition to forming chain-like defect, can induce displacing of one nearest lattice atom and forms a small vacancy-interstitial-vacancy complex, which increases the vacancy numbers. At longer times, majority of these boundary defects will be removed through defect annihilation.

To show the dependence of E_{min}^{V} and E_{min}^{I} patterns on boundary configurations, **Fig** 23. plots the energy mapping of E_{f}^{V} and E_{f}^{I} over symmetric tilt grain boundaries of three different angles, with $\theta = 8.8°$ for $(0113)[100]\Sigma = 85$ (**Fig 23 (a)**), $\theta = 36.86°$ for $(013)[100]\Sigma = 5$ (**Fig 23 (b)**), and $\theta = 53.13°$ for $(012)[100]\Sigma = 5$ (**Fig 23 (c)**). Viewed along the rotation axis forming symmetric boundary, i.e. the direction perpendicular to planes shown in **Fig 20 (b)**, E_{min}^{I} regions are periodically spaced with separation distances decreasing with increasing boundary angles, the same as E_{min}^{V} regions. The neighboring interstitial-vacancy pairs on the GBC defect cannot be separated more than, roughly, one lattice spacing distance, which means for small angle boundary ($\theta = 8.8°$, **Fig 23 (a)**), the separation distance between neighboring E_{min}^{I} (or E_{min}^{V}) sites is too large, and the GBC defect can only form along the rotation axis, since this direction guarantees one E_{min}^{I} or one E_{min}^{V} sites over every plane distance.

Each E_{min}^{I} and E_{min}^{V} region contains, usually, multiple sites for interstitials or vacancies to occupy, which leads to zigzag like configurations of GBC defect. A GBC defect can form on the same plane (The 1st or 2nd planes denoted in **Fig** 22 (b)) if neighboring $E_{min}^{I} - E_{min}^{V}$ pairs on the plane has a separation distance comparable to one lattice spacing, which occurs only for large angle boundary, $\theta = 53.13°$ (**Fig** 23 (c)). In comparison with small angle boundaries, very large angle boundary leads to higher E_{min}^{I} (or E_{min}^{V}) densities and provides more GBC defect formation directions.
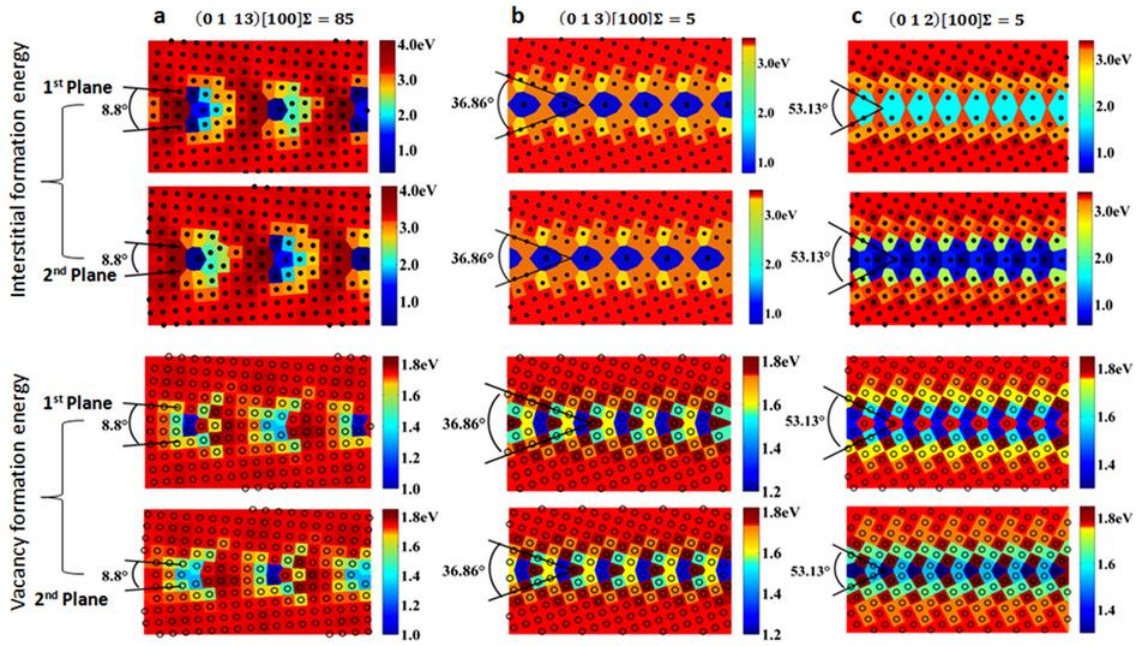

Fig 23: Formation energy of interstitials and vacancies in the bulk and at the boundaries, created with tilt angles of (a) 8.8°, (b) 36.8°, and (c) 53.13°, respectively.

The energy scale bar is provided. The hollow circles refer to vacancies and the solid circles to interstitials. These interstitials sites are not octahedral and tetrahedral

interstitials since both are not energetically favorable. For interstitials in the bulk, energy minimization favors dumbbell defect formation around one lattice location. Close to the boundary, isolated interstitials become energetically favorable to form and corresponding stable locations are identified by allowing structural relaxations in simulations.

4.5 Summaries

Understanding radiation responses of Fe-based metals is essential to develop radiation tolerant steels for longer and safer life cycles in harsh reactor environments. Nanograined metals have been explored as self-healing materials due to point-defect recombination at grain boundaries. The fundamental defect-boundary interactions, however, are not yet well understood. We discover that the interactions are always mediated by formation and annealing of chain-like defects, which consist of alternately positioned interstitials and vacancies. These chain-like defects are closely correlated to the patterns of defect formation energy minima on the grain boundary, which depend on specific boundary configurations. Through chain-like defects, a point defect effectively translates large distances, to annihilate with its opposite, thus grain boundaries act as highly efficient defect sinks that cannot saturate under extreme radiation conditions.

CHAPTER V

ATOMIC UNDERSTANDING OF DEFECT ANNIHILATION AT GRAIN

BOUNDARIES IN ALPHA-FE

5.1 Introduction

In last chapter we focus on the mechanism of defect trapping by a grain boundary through chain like defect. Now we proceed to understand the mechanism of annihilation/recombination of defects loaded on a grain boundary. Defect loading towards a grain boundary represents only the first step of defect removal. If the second step, defect removal at a grain boundary, is difficult and requires high energy barrier, then it is expected that defect sink strength of grain boundaries will be reduced or disappeared, since the stress fields induced by over-loaded defects at grain boundary will make defect formation energy at boundaries higher than that in bulk, leading defect rejection from the boundary regions. Assuming that both vacancy and interstitial defects are randomly loaded at a grain boundary, the subsequent interstitial-vacancy recombination must involve defect transport, of which the mechanism is largely unknown.

5.2 The Effectiveness of Annihilation Defects for GBs with Different Misorentation Angles

Fig 24 (a). shows the snapshots of MD simulations of defect-loaded grain boundaries of different boundary misorientation angles. The defects are randomly created through Fe self ion bombardment in the cell and a fraction of them are loaded towards the boundaries. At time 1ns after the bombardments, majorities of boundary defects are removed at large angle boundary. In a comparison, the defect removal efficiency turns to low for small angle boundary. Furthermore, surviving defects exhibit certain patterns. For small angle boundary, interstitials and vacancies form straight one dimensional chain defects. Carful comparison with calculated defect formation energy mapping at boundary shows that these defects correspond to the sites of energy minima. That is, interstitial defects in a chain correspond to the sites of interstitial formation energy minima of boundaries, and vacancies in a chain correspond to that of vacancy formation energy minima. On the right side, as shown in **Fig** 24(b), we compared the formation energy minima patterns under different misorientation angles. For clarification, only formation energy of interstitials of the first monolayer and formation energy of vacancies of the second monolayer are plotted. The arrows specify the direction of chain defects. Due to structural differences under different angles, exact locations and line density of these formation energy minima are different, leading to different chain configurations. For large angles, the chain is almost a straight line consisting of alternately positioned interstitials and vacancy. For small angle, story is more complicated. There are two types of chain

defects. One is similar to that formed at high angle grain boundary with alternately positioned interstitials and vacancies. Anther has periodic zig-zag feature and the line density of interstitials are twice of that of vacancies.

As shown in **Fig**. 24, the zig-zag chain defects created for small angles are relatively immobile. After 1ns annealing, they barely move. For these chain defects, interstitial numbers are twice of that vacancies, therefore, they cannot form by structural relaxations in a defect free zone. We can call them a "locked chain defect". This is very different from other chain defects which can easily form by structural relaxation of an originally defect-free region between a well separated interstitial and vacancy, since the number of interstitial is equal to that of vacancy and the net defect is zero. These chain defects are unlocked and can move freely. For example, if the interstitial at one end of the chain occupies the vacancy site next, the chain length is reduced. On the other end of the chain, a lattice atom next to the end can create another vacancy-interstitial pair which increases the chain length. Therefore, the chain moves one step along the chain direction. This, in fact, is what observed from our MD simulations. Such chain moving mode can be used for the "locked chains" created at small angle boundary.
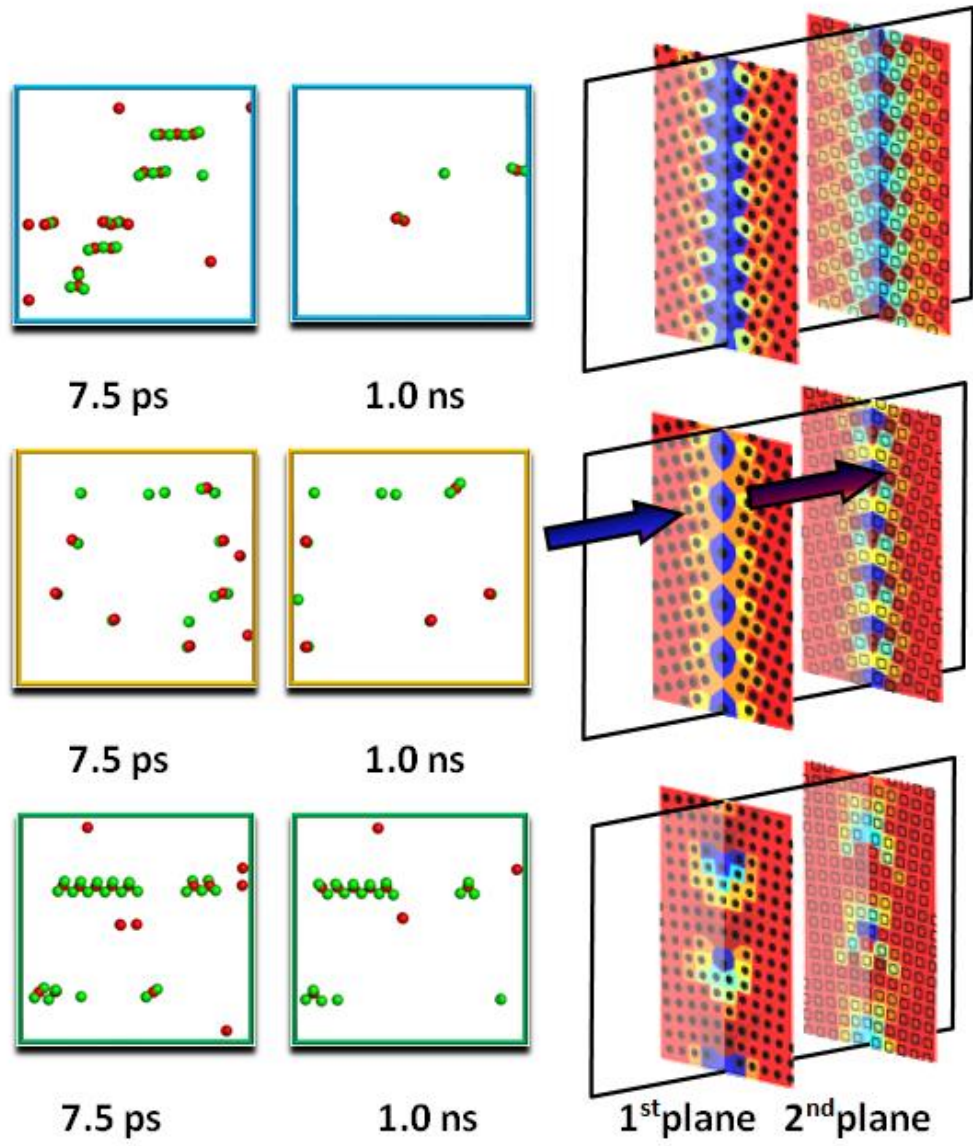
(a)   (b)

Fig 24. The snapshots of MD simulations of defect-loaded grain boundaries of

different boundary misorientation angles.

The next question is how these unlocked chain are formed at small angle boundary. First of all, they are consequence of the one dimensional agglomeration of interstitial type defects. For one interstitial loaded on a grain boundary, instead of direct jumping among interstitial site, it induces unlocked short chain and moves freely along one direction. If this mobile defect meets another interstitial defect, they merge and change into a short unlocked chain. The process repeats and leads to the formation of the long unlocked chain observed in **Fig 24**(a). for small angle boundaries.

The next question is why there is no such unlocked interstitial-rich chain defect observed for large angle. There is a fundamental reason behind that. For small boundary angle, the stress fields are strong and there are "deep" energy minima for interstitial sites, which correspond to the interstitial sites in mobile unlocked chains. There are also "second deep" energy minima which have formation energy slightly higher than that of the lowest energy minima. From the view point of structural relaxation and stress filed cancelation around a vacancy, there are two ways: one is to form straight mobile chain in which one vacancy is surrounded by two neighboring interstitials (occupying the lowest energy minima) to reduce stress fields; another is to form unlocked zig-zag chain in which one vacancy is surrounded by three neighboring interstitials (occupying the second lowest energy minima) to reduce the stress fields. For large angle boundaries, interstitial formation energy of "deepest energy minima" is systematically higher than of small angle

boundaries, and the energies of the "second to the deepest" are even higher. So the stress field release using "second to the deepest" is not energetically favorable.

Fig 25.shows the movements of short chain defects created on a small angle boundary, and how an interstitial-vacancy recombination is realized by using such a chain to move the interstitial closer to a vacancy. At time 2.5ps, one separated interstitial-vacancy pair is loaded on the boundary. At time 15.9ps, the interstitial creates a short chain and move one step closer. At time 16.55 ps, a lattice atom between the interstitial-vacancy pair "splits" into another interstitial-vacancy pair in the middle. At time 17.05 ps, a chain is formed. This transition also shows the difference between a chain defect and a crowdion defect. The crowdion defect is created under damage cascade stage and is caused by sequential knocking-on events along the atom row direction. In other words, crowdion forms by a more violent process requiring energy transfer larger than the displacement energy. In a comparison, the chain defect is formed as a result of structural relaxation requiring much less energy barrier. There is no necessity of time sequence. For example, our modeling once noticed the event that short chain is induced in the middle of a well separated interstitial-vacancy pair, instead of being initialized form either interstitial or vacancy.

2.5ps   15.9ps   15.95ps

16.55 ps   17.05ps   17.2ps

18ps   Small angle 8.8° $(0-1\ 13)[100]\Sigma = 85$
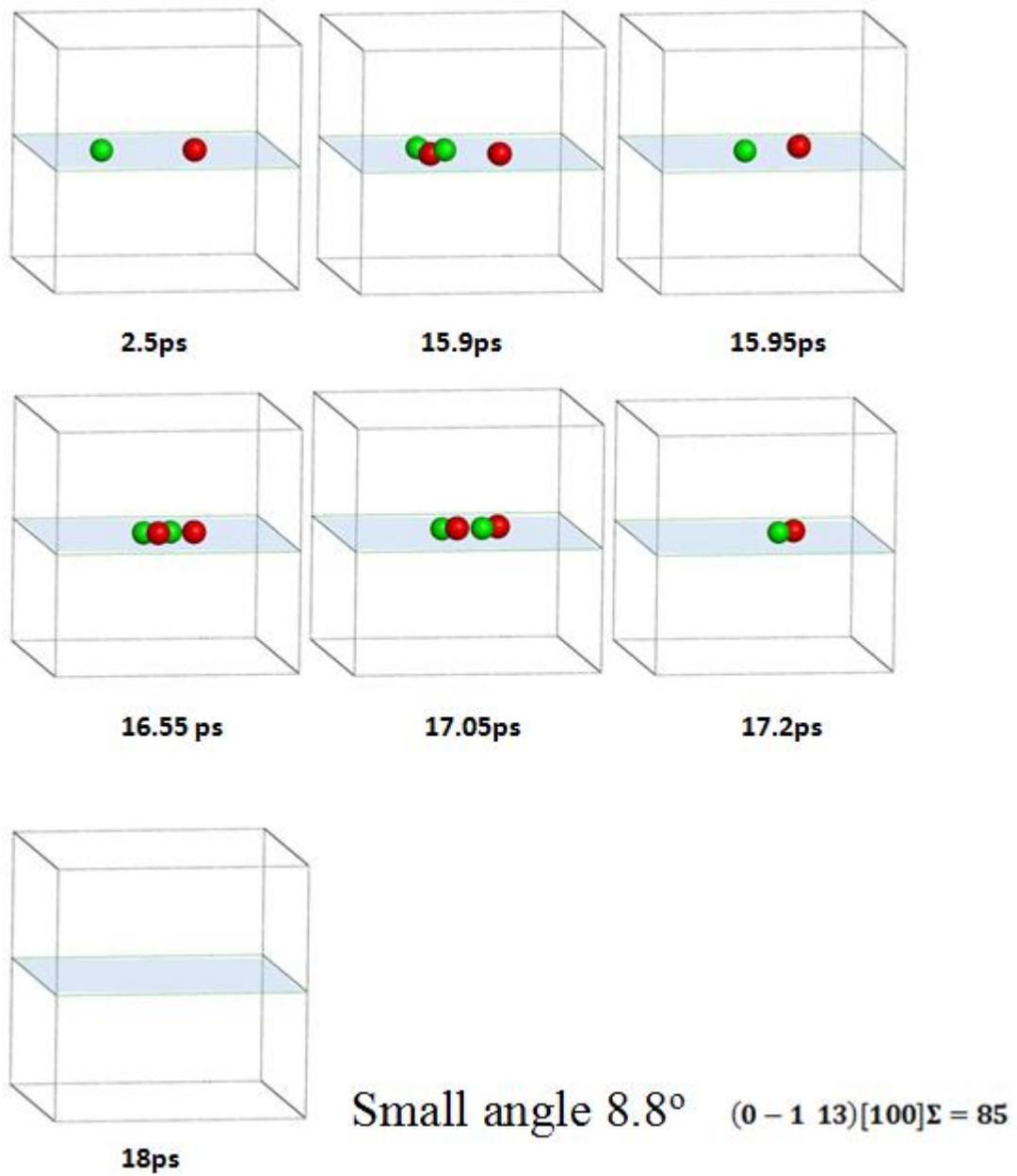
Fig 25 Chain defects created on a small angle boundary

Fig 26 shows a more complicated mechanism, which occurs only for large angle grain boundary. At time 3.1 ps, there is a pair of interstitial and vacancy, which are located at different chain direction. For small angle boundary, such defect pair will not have interactions since allowable moving directions for each are parallel to each other. However, the large angle boundary has a unique way to annihilate defects. At time 6.23 ps, interstitial moves by forming a short chain defect. At time 6.43 ps, this chain increases the length by displacing one lattice atom ahead of the chain end into the favorable interstitial site. At time 6.48 ps, the neighboring interstitial-vacancy pair at the other end of the chain has recombination, which is equivalent to move the chain one step close to the vacancy. Then, at time 7.1 ps, another chain defect forms which points to the vacancy. At 7.15 ps, the chain shrinks through interitial-vacancy recombination. At time 7.2 ps, recombination completes.

3.1ps   6.23ps   6.43ps

6.48ps   7.1p   7.15ps

Large Angle 53° $(0-1\ 2)[100]\Sigma = 5$

7.2ps
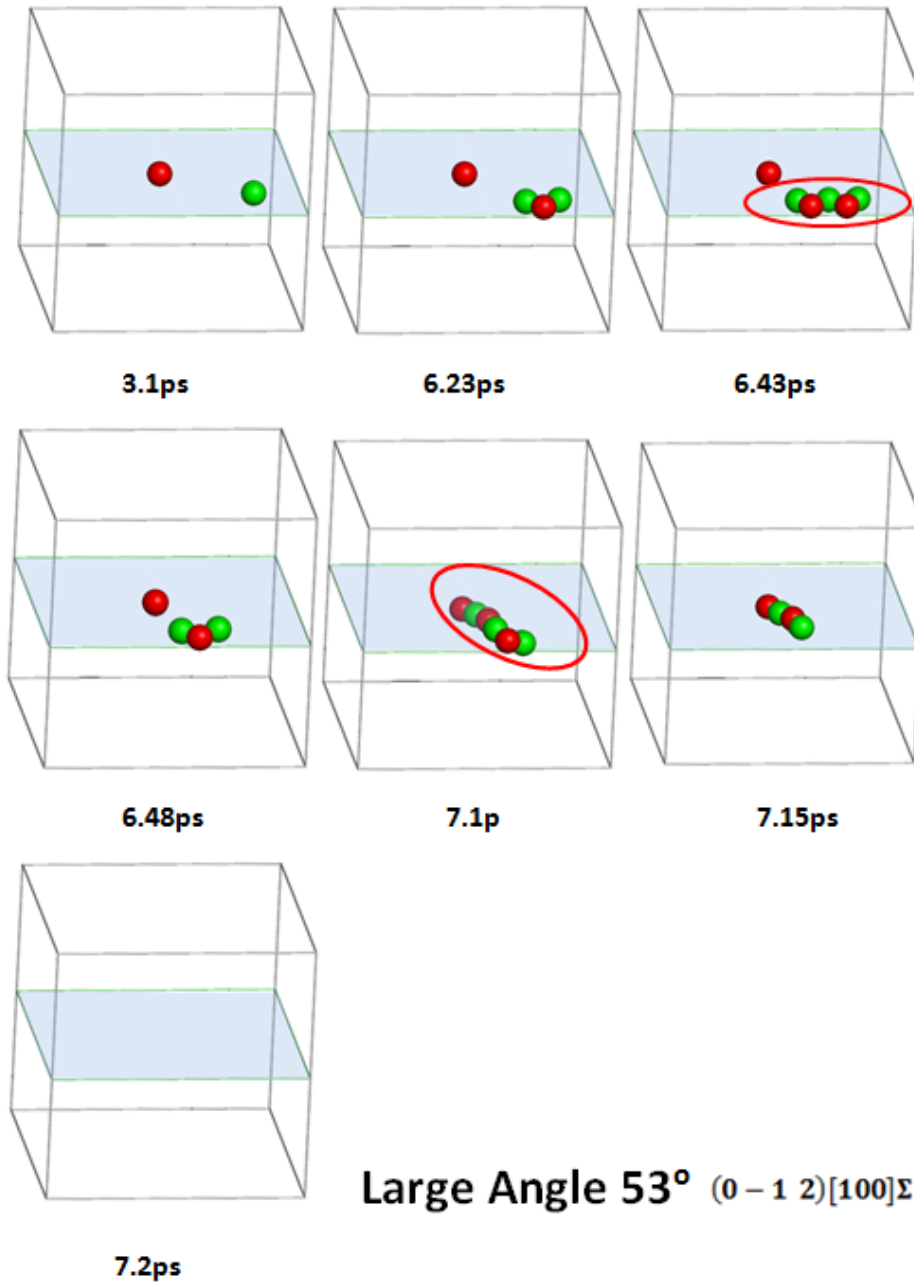
Fig 26 Defects annihilation on a large angle boundary

62

The most important finding from **Fig**. 26 is that the chain can form crossing over the direction of rotating axis to form the grain boundary. In other words, its direction is different from the chain direction created at small angle boundary. Careful examination shows that the chain is formed by selecting defects from different parallel chains. This is possible only for large angle boundary, in which the energy minima density is high that energy minima from neighboring parallel chains begin to touch each other. Therefore, for alternately positioned interstitial and vacancies required to form the chain, interstitial can be picked from one chain and vacancy can be picked from the next chain. The most significance here is that for large angle boundary, allowable chain defect formation directions become more than that of small angle boundary. For small angle boundary, only one direction is allowed. For large angle boundary, chains can select from a two dimensional plane.

What happens for medium angle, which has a higher density of chain directions than small angle, but its chain density is not high enough to allow new chain direction created like large angle boundary? As shown in **Fig.** 27, our modeling noticed a unique defect recombination way for medium angle boundary. At time 3.9 ps, a pair of interstitial and vacancy is located at different chain directions. At time 4.68 ps, the vacancy is able to induce the formation of a chain shooting towards the bulk. This chain leaves the boundary plane. The chain direction is along the <111> direction in Fe, which represents the direction having the highest linear atomic density. This makes sense since for the direction having a low linear density, the displacement of lattice atom into an interstitial

will have small effect to induce the displacement of next lattice atom. At time 4.7 ps, recombination along the chain occurs which creates a vacancy in the bulk. Next, at time 4.75 ps, a new interstitial-vacancy pair is created, with the vacancy in the bulk. Next, at time 4.78 ps, a chain defect is induced between bulk vacancy and boundary interstitial. At time 4.95 ps, defect recombination finishes.
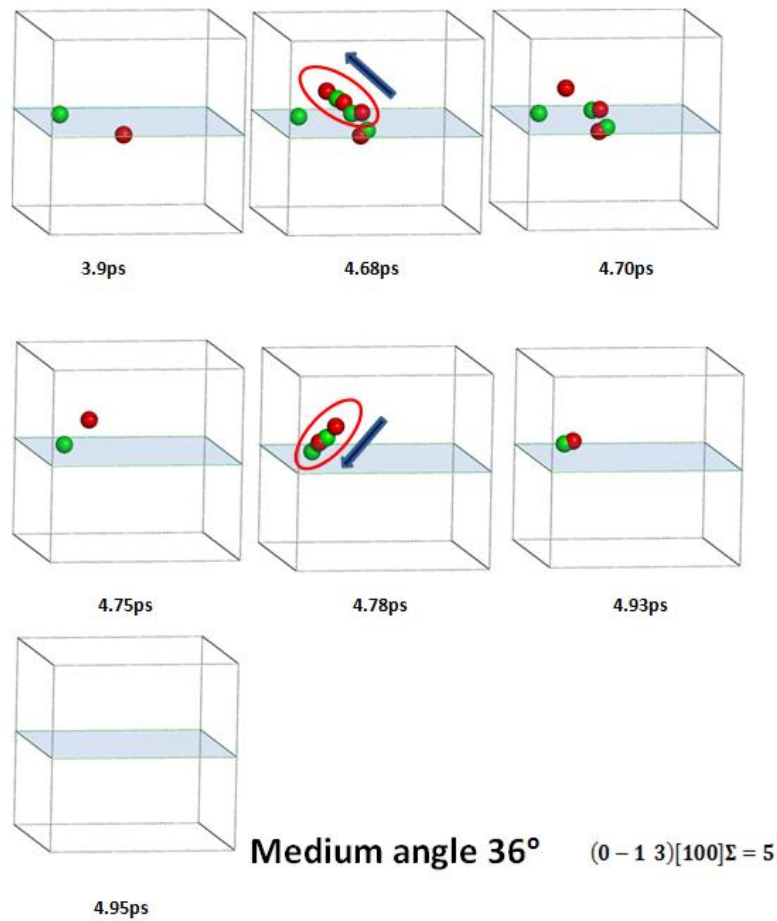
Fig 27 Defect recombination way for medium angle boundary

In order to shed light onto the chain defect mediated defect annihilation proces, we calculated the energy required to achieve complete defect removal. **Fig** 28 plots the calculated energy barriers for chain defects created under different boundary misorientation angles. The energy barriers slightly vary in the range of 0 eV to 1.5 eV. Considering the statistics, there is no a clear trend that the energy barriers have strong dependence on angles. The inset shows the definition of energy barrier in the process. Starting from the formation of a chain like defect, the subsequent structural relaxation required for annihilation of neighboring interstitial-vacancy pair needs to over an energy barrier, which represents the energy height difference between the starting status and saddle points having largest stress fields. When defect recombination is finished, the potential energy reaches the lowest value, defined as the zero in the figure.
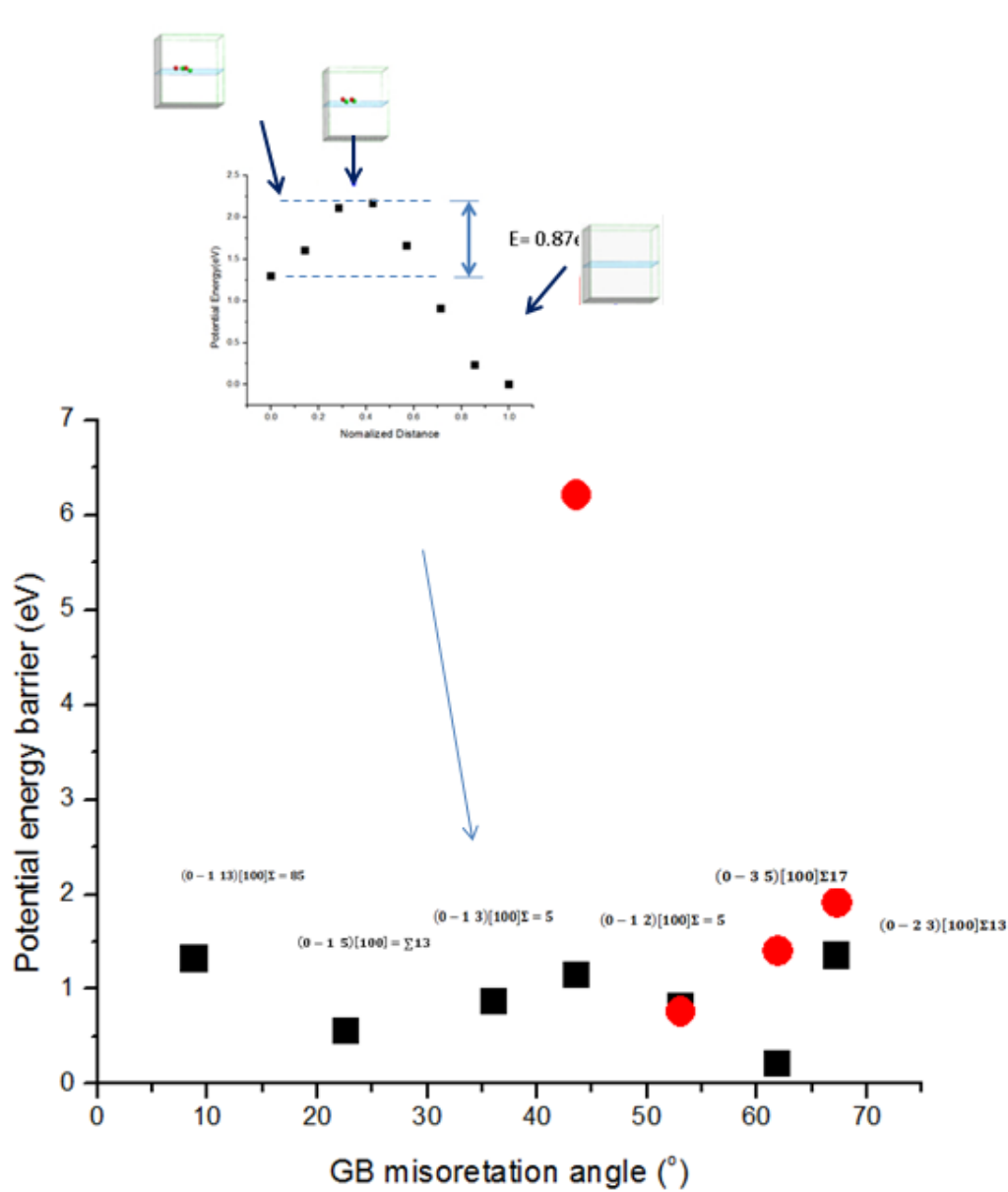
Fig.28 Energy barriers for chain defects created under different boundary misorientation angles

**Fig**.28 further plots the energy barrier of cross chains, which represent new chain directions available only under large angle boundaries. At large angles, the required activation energies are comparable to that of other aligned chains. However, at relatively smaller angles, the energy barriers become extremely high. This is due to the fact that under smaller boundary misorientation angles, the linear density of parallel chains decrease with increasing angle. Therefore the distances between neighboring interstitials and vacancies pair, on the same cross chain, become larger. An interstitial needs to move relatively longer distance and overcome larger energy barrier to occupy the neighboring vacancies in the annealing process.

If energy barriers do not have significant differences between aligned strains and cross strains, then the efficiency in defect removal is primarily influenced by the number of allowable annealing paths. There are two major factors determining the direction number. One is the grain boundary misorientation angles. The higher the angles, the larger the number of parallel aligned chain directions. **Fig** 29. summarizes the distance between two neighboring parallel chains. The distances first decrease with increasing angles and then become increase at larger angle region. The other factor is the creation of cross chains once the angle is larger than a critical number such that the original parallel chains begin to touch each other. The number increase is close to a step height profile and, beyond the critical angle, the direction changes from one to three. The newly added two directions are about 45 degrees and 135 degrees away from the original chain direction.
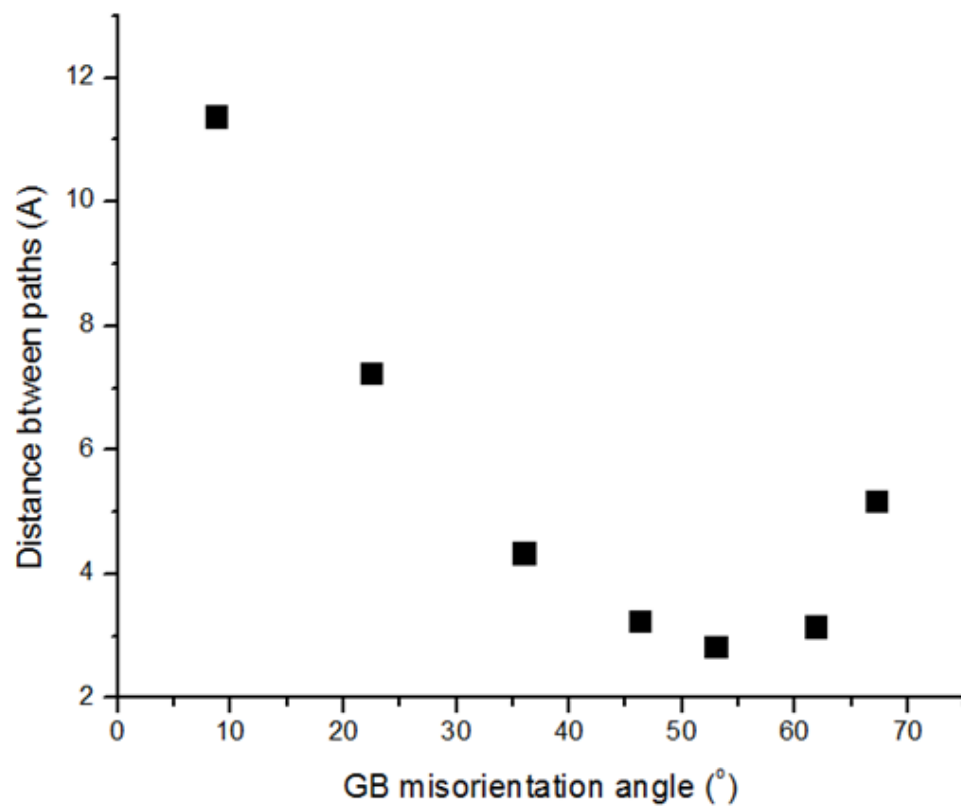
Fig 29. Distance between two neighboring parallel chains

The above findings are very important to understand the upper limits of defect sink strengths under high dpa irradiation. The sink strength is determined by two factors: one is the strength change of boundaries and the other is structural integrity of boundaries. Under heavy ion irradiation, damage cascades created near a boundary will create interface mixing thermally and athermally. The thermal mixing is caused by enhanced point defect migration under temporally increased temperature, due to thermal spike formation. Since thermal spikes typically can reach temperature much higher than the melting points of materials, the interface mixing can be treated as liquid diffusion and liquid mixing at a short time scale. The athermal effects come from ballistic collisions in which energetic atoms injected from the damage cascade core behave more like low energy ion irradiation, and can easy penetrate through the boundary and cause mixing. These two mixing mechanisms will cause boundary structural integrity. As for the strength change, if defect trapping and migration towards a grain boundary is biased, i.e., interstitials diffuse faster than that of vacancies, sink strength expects to be quickly saturated. By trapping only one type of defects, defect annihilation cannot be realized and the quick buildups of stress fields will force turn of sink properties. Even a boundary can effectively trap bot interstitial and vacancy defect types, the sink strength is determined how efficiently the previously loaded defects get annihilated. Otherwise, the unannealed defects at the boundary will turn off sink properties as well.

To study the sink strength limits, we did MD simulations by keep bombarding a cell with higher and higher ion fluences. This is realized by several repeated defect

introduction process. First, 100 atoms randomly selected from the cell are assigned with an energy of 100 eV with

Momentum directions randomly selected. Then the structure is relaxed for about 100ps to achieve stable defect configurations and vacancy defect mapping is extracted. Then, another 100 atom bombardment is applied, following by another structural relaxation for another 100 ps. **Fig** 30. shows the interstitial defects created by one bombardment step (irradiated by 100 atoms), three bombardment steps (irradiated by 3×100 atoms), and five bombardment steps (irradiated by 5×100 atoms), respectively. We used ion bombardment, instead of introducing point defect by randomly displacing lattice atoms, for a better simulation of damage cascade creation in reactor environments. The irradiated cell contains a large angle grain boundary in the center and the microstructure is featured with a defect denuded zone. The width of the zone is 23Å after the first bombardment step, and is 18 Å after three bombardment steps, and is 17 Å after five bombardment steps. This observation suggests that the boundary defect sink strength is reduced at higher damage levels.
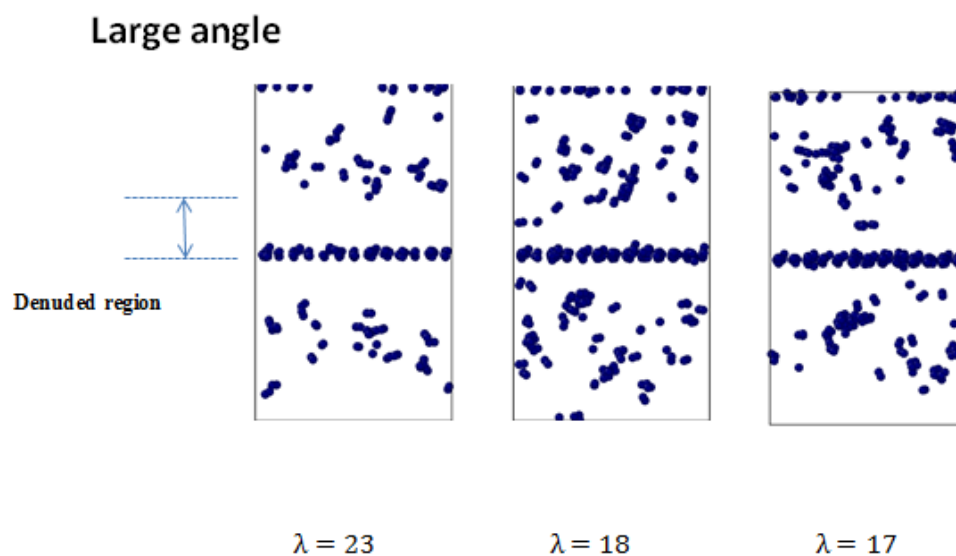
Fig 30. The interstitial defects after bombardment near large angle GB

Fig.31 shows the defect mapping in the cell containing a medium angle grain boundary. The width of the defect denuded zone keeps at 14Å after one, three, and five bombardment steps. This suggests that sink strength is not degraded by the bombardment. The behavior is different from the large angle grain boundary since the latter shows reduced widths. A rough estimation on the amount of removed defects can be made by integrating the total disappeared defects over the denuded region, which is, neglecting the details of unit, 500 bombardments×dpa/bombardment×14 for the highest damage level for the medium boundary angles. In other words, upon absorbing that number of defects, the sink strength is not saturated.

Medium angle

$\lambda = 14$ $\lambda = 14$ $\lambda = 14$
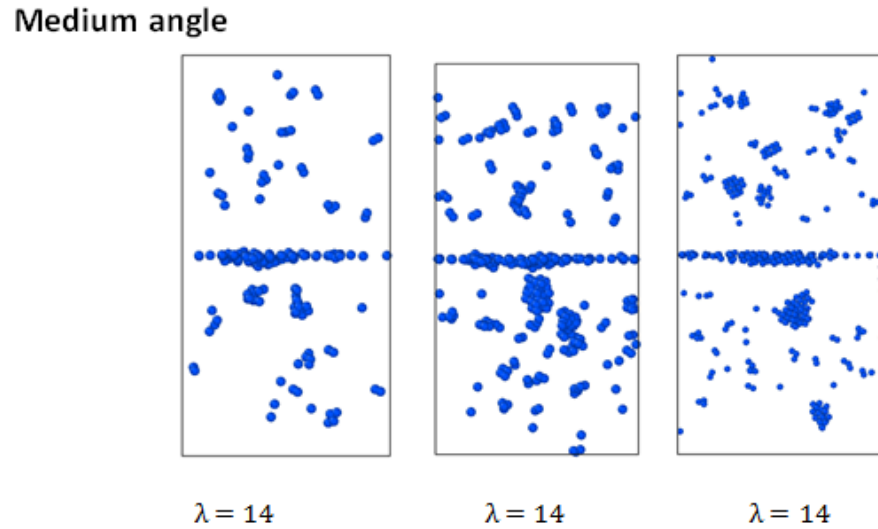
Fig 31. The interstitial defects after bombardment near medium angle GB

In a comparison, for large angle grain boundary, width change or sink strength changes are observed after three bombardments, corresponding to 300 bombardments×dpa/bombardment×17. Therefore, we can conclude here that, the sink strength of large angle grain boundaries is larger than that of medium angle grain boundaries, as judged by the width differences after the first bombardment (23Å vs. 14Å). However, the sink tolerance of larger angle grain boundaries is poor than that of medium angle grain boundary, as judged by defect numbers which begin to cause width changes.

For small angle grain boundary, it has not only weaker defect strength but also weaker radiation tolerance. As shown in Fig 36, the widths of denuded zones are 10Å, 5Å, and 2Å, after one, three and five bombardment steps. For the first bombardment step, the width of 10Å is the shortest when compared with the medium and large angle grain boundaries, meaning the weakest defect trapping/annihilation capabilities. After three bombardment steps, the width changes from 10Å to 5Å, suggesting that defect sink strength begins to be saturated at the damage levels of 300 bombardments×dpa/bombardment×5.

Small angle

$\lambda = 10$ $\lambda = 5$ $\lambda = 2$
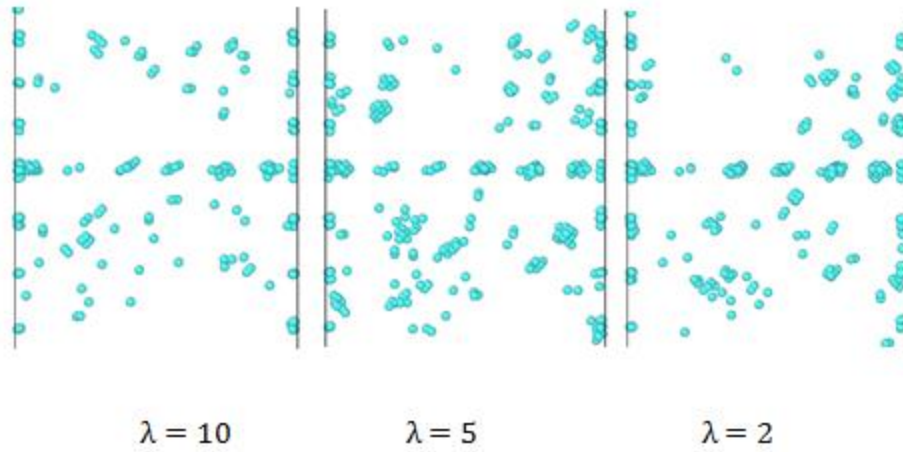
Fig 32. The interstitial defects after bombardment near small angle GB

Our studies clearly show that defect sink strength increases with increasing grain boundary misorientation angles. However, the radiation tolerance of grain boundary may show a maximum at medium angle. We believe the above two behaviors are caused by the following fundamental reasons. First, larger angles are always better than small angles for both defect loading and defect annihilation. The density of formation energy minima determine not only how many sites to load defects from the bulk but also how many chain like defects can be created to annihilate defects. However, considering that energy barrier still needs to be overcomed to recombine defects, a strong defect trapping capability may lead to quickly accumulated defects which are not recombined. Thus defect sink strength is reduced at large angle grain boundaries. The study also suggests that the overall defect removal efficiency relies on the rate of defect creation efficiency. Our modeling agrees with the early experimental observations from helium irradiated copper. As a function of boundary misorientation angles, the widths of defect denuded zones increase and then decrease with increasing boundary angles, having a maximum in the medium angle.

CHAPTER VI

CONCLUSION

Our studies discussed atomic scale details of defect-grain boundary interactions. At the beginning, our experiment showed that ultra-fine grain iron structures have significant strength to suppress void formation, as shown in Chapter IV. In order to understand mechanisms behind this, MD simulations were performed.

Firstly, The MD results of radiation damage indicate that GBs act as defect sinks during irradiation, which is in agreement with experimental observation. However, defect annihilation at a grain boundary is complicated; therefore it is very difficult to extract information from radiation damage in MD simulations. We then simplify the simulation to an interaction between point defects and GBs.

Based on MD simulation results, we have shed light into atomic scale interactions between point defects and GBs. After collecting a large amount of events, chain-like defects were recognized to be a key factor that assists point defects trapping at GB. Three types of chain-like defects were observed: bulk chain-like, grain-boundary chain like and bulk chain-like and rain-boundary chain like defects. We found that defect recombination efficiency is enhanced greatly via these chain-like defects. Particularly, we noticed that recombination through grain-boundary chain like defects corresponds to vacancy and intestinal formation energy configuration, which is critical for GB radiation tolerance. Moreover, such configurations restrict defect migration along specific channels.

In Chapter V, we investigated defect recombination via grain boundary chain-like defect sensitivity to GB misoreintation angles. After a series of calculation, the results presented that defect moving directions and their associated energy barriers are dependent on GB misoreintation angles. Specifically, we observed that defects can penetrate though these channels at large angles, leading to enhancement of defect annihilation.

REFERENCES

1   J. Mansur, Nucl. Mater.216, 97 (1994)

2   Cawthorne and Fulton, Nature, 216, p. 575 (1965)

3   G.S. Was, Fundamentals of radiation materials science: metals and alloys, Springer, New York, 2007

4   B. D. Wirth, Science 318, 923 (2007)

5   M. J. Demkowicz, R. G. Hoagland, J.P. Hirth, Phys. Rev. Lett. 100, 136102 (2008)

6   E.G. Fu, A. Misra, H. Wang, L. Shao and X. Zhang, J. Nucl. Mater. 407, 178 (2010)

7   X-M Bai et al., Science 327, 1631 (2010)

8   Y. Chimi et al., J. Nucl. Mater. 297, 355 (2001)

9   Blas Uberuaga, Los Alamos National Laboratory, private communications (2006)

10   M. Rose, A. G. Balogh, H. Hahn, Nucl. Instrum. Methods Phys. Res. B 127-128, 119 (1997)

11   Alder, B. J.; T. E, J. Chem. Phys. 31 (2) 459 (1959)

12   A. Rahman, Phys Rev 136 (1964)

13   Lennard-Jones, J. E. Proc. R. Soc. Lond. A106 (738) 463–477 (1924)

14   Daw, Baskes, Phys Rev Lett, 50, 1285 (1983)

15   Daw, Baskes, Phys Rev B, 29, 6443 (1984)

16   Finnis, Sinclair, Philosophical Magazine A, 50, 45 (1984)

17   Ackland, Condensed Matter,17,1851 (2005)

18   Ackland, Mendelev, Srolovitz, Han and Barashev, Journal of Physics: Condensed Matter, 16, S2629 (2004)

19   Stukowski, Modeling Simulation Materials Science & Engineering, 7, 075005 (2009)

20   LAMMPS Molecular Dynamics Simulator. Sandia National Laboratories. Retrieved 2010-10-03.

21   Han et al., Acta Materialia 60, 6341 (2012)

22   M. Haouaoui, K.T.Hartwig, E.A.Payzant,ActaMater,53 (2005)

23   I Charit, K. L Murty, JOM 62, 67–74 (2010)

24   P Yvon, J. Nucl. Mat. 385, 217–222 (2009)

25   B. D. Wirth, V. Bulatov, J. Nucl. Mat. 283–287, 773–777 (2000)

26   N. Nita, R. Schaeublin, J. Nucl. Mater. 329–333, 953–957 (2004)

27   K. Arakawa,. et al. Science 318, 956–959 (2007)

28   N. Soneda, T. Phil. Mag. A 78, 995–1019 (1998)

29   C. Cawthorne, E. J. Fulton, Voids in irradiated stainless steel. Nature 216, 575–576 (1967)

30   T. Diaz de la Rubia. et al. Nature 406, 871–874 (2000)

31   B. N Singh, A. J. E. Foreman, H. J. Trinkaus, Nucl. Mater. 249, 103–115 (1997)

32   M.Samaras, P. M. Derlet, H. V. Swygenhoven, M.Victoria, Phys. Rev. Lett 88, 125505 (2002)

33   D. A. McClintock, M. A. Sokolov, D. T. Hoelzer, R. K. Nanstad, Mechanical. J. Nucl. Mater. 392,353–359 (2009)

34   C.Saldana, T. G.Murthy, M. R Shankar, E. A. Stach, , S.ChandrasekarAppl. Phys. Lett. 94, 021910 (2009)

35   T.Chookajorn, H. A. Murdoch, C. A. Schuh, Science,337, 951–954 (2012)

36   H. Ogawa, GBstudio . Materials Transactions 47, 2706–2710 (2006)

37   S.J. Plimpton, J. Comp. Phys. 117, 1 (1995)

38   M.I. Mendelev, et al. Phil. Mag. 83, 3977-3994 (2003)

39   H.R. Paneth, Phys. Rev. 80, 708-711 (1950)

40   D. Chen, L. Shao, Nucl. Instrum. Methods Phys. Res. B 272, 33-36 (2012)

APPENDIX A

1) Input file of initial relaxation

```
#Initialization^M
clear
units metal                     # Units to be used for simulation^M
dimension 3                     # Dimensions of space for
simulation. 3D is default

newton on on                    # Newton's 3rd law for pairwise and
bonded interact


                                # Processors n m o define the proc.
grid^M
boundary p p p                  # Rules or boundary^M
atom_style atomic               # Rules for atom styles. Atomic is
default^M
                                # atom_modify^M

# Atom definition




read_data datafile.lammps




#Settings^M



pair_style eam/fs
pair_coeff * * Fe_mm.eam.fs Fe

lattice bcc 1

timestep 0.005

thermo 100


min_style cg
```

```
minimize 1.0e-8 1.0e-8 100000 100000

reset_timestep    0



velocity all create 600 565435 rot yes dist gaussian


fix        0   all npt temp 500 500 10 aniso 0 0 10

run        25000

unfix 0



fix        1   all nvt temp 500 500 0.2 drag 0.2

dump atom all xyz 5000 output.xyz


run        25000


unfix 1



write_restart restartfile
```

2) Input file of radiation simulation

```
#innitialization
clear
units metal
dimension 3                    # Dimensions of space for
simulation. 3D is default
newton on on                   # Newton's 3rd law for pairwise and
bonded interactions

                               # Processors n m o define the proc.
grid
boundary p p p                 # Rules or boundary
atom_style atomic              # Rules for atom styles. Atomic is
default
```

```
                                   # atom_modify



# Atom definition

read_restart restartfile              #from relaxation


lattice bcc 1

reset_timestep  0



#Settings


pair_style eam/fs
pair_coeff * * Fe_mm.eam.fs Fe



fix 1 all nve

set atom 250001 x -5 y 70.3 z 71

velocity id1 set 1005.6 157.312 0



thermo 50
timestep 0.0002



dump atom all xyz 250 radiation.xyz



run 25000
```

```
unfix 1

write_restart restartfile          #after radiation
```

3) Input file of annealing

```
#innitialization
clear
units metal
dimension 3                    # Dimensions of space for
simulation. 3D is default
newton on on                   # Newton's 3rd law for pairwise and
bonded interactions

                               # Processors n m o define the proc.
grid
boundary p p p                 # Rules or boundary
atom_style atomic              # Rules for atom styles. Atomic is
default
                               # atom_modify


# Atom definition


read_restart restartfile       # restart file after radiation

lattice bcc 1


#Settings


pair_style eam/fs
pair_coeff * * Fe_mm.eam.fs Fe



fix 11 all nve



thermo 100
timestep 0.005
```

```
dump atom all xyz 1000 fe-500ps-standard.xyz
#dump atoms all custom 200 fe-10ps id type x y z c_1

run 99000


unfix 11
```

APPENDIX B

C++ code for characterizing point defects

```cpp
#include <fstream>
#include <iostream>
#include <math.h>
#include <vector>
using namespace std;

float rad = 0.8275,range=26;
float stable = 0.5;
float maxx=13;
float maxy=13;
float maxz=13;
float minx = -13;
float miny = -13;
float minz = -13;
float sBox = -13;
float eBox = 13;
float coe = 0;
//int SK = 2;
//int step = 5;
void main()
{
        char filename[] = "data/targetfile.xyz";
        char firstFrame[] = "data/standadfile.xyz";
        char savefilename[] = "data/fileusedforPymol.SEG";
        char savefilename2[] = "data/defectnumber.txt";

        char NumString[20];
        char keyword[256];
        int Num, temp, n=0,count=0;
        float posx,posy,posz;
        float posxx,posyy,poszz;
        float nposx,nposy,nposz;
        float dis,dis1,dis2,dis3;
        float min,max;
        vector<float> px,py,pz;
        vector<float> tx,ty,tz;
        vector<float> cx,cy,cz;
        vector<int> sphereStat;
        vector<int> atomStat;
        ifstream is(filename, ios::in);
        ifstream sds(firstFrame, ios::in);
        ofstream ofs(savefilename,ios::out);
        ofstream ofs2(savefilename2,ios::out);
        ofs<<"from pymol.cgo import *"<<endl;
        ofs<<"from pymol import cmd"<<endl;
        ofs<<"box = ["<<endl;
        ofs<<"LINEWIDTH, 1.0,"<<endl;

        ofs<<"BEGIN, LINES,"<<endl;
```

```cpp
ofs<<"COLOR, 0.8, 0.8, 0.8,"<<endl;
ofs<<"VERTEX,"<<eBox<<","<<eBox<<","<<eBox<<","<<endl;
ofs<<"VERTEX,"<<eBox<<","<<sBox<<","<<eBox<<","<<endl;
ofs<<endl;
ofs<<"VERTEX,"<<eBox<<","<<eBox<<","<<eBox<<","<<endl;
ofs<<"VERTEX,"<<eBox<<","<<eBox<<","<<sBox<<","<<endl;
ofs<<endl;
ofs<<"VERTEX,"<<eBox<<","<<eBox<<","<<eBox<<","<<endl;
ofs<<"VERTEX,"<<sBox<<","<<eBox<<","<<eBox<<","<<endl;
ofs<<endl;
ofs<<"COLOR, 0.5, 1.0, 0.5,"<<endl;
ofs<<"VERTEX,"<<sBox<<","<<sBox<<","<<sBox<<","<<endl;
ofs<<"VERTEX,"<<sBox<<","<<eBox<<","<<sBox<<","<<endl;
ofs<<endl;
ofs<<"VERTEX,"<<sBox<<","<<sBox<<","<<sBox<<","<<endl;
ofs<<"VERTEX,"<<sBox<<","<<sBox<<","<<eBox<<","<<endl;
ofs<<endl;
ofs<<"VERTEX,"<<sBox<<","<<sBox<<","<<sBox<<","<<endl;
ofs<<"VERTEX,"<<eBox<<","<<sBox<<","<<sBox<<","<<endl;
ofs<<endl;

ofs<<"COLOR, 0.8, 0.8, 0.8,"<<endl;
ofs<<"VERTEX,"<<eBox<<","<<sBox<<","<<eBox<<","<<endl;
ofs<<"VERTEX,"<<sBox<<","<<sBox<<","<<eBox<<","<<endl;
ofs<<endl;
ofs<<"VERTEX,"<<eBox<<","<<sBox<<","<<eBox<<","<<endl;
ofs<<"VERTEX,"<<eBox<<","<<sBox<<","<<sBox<<","<<endl;
ofs<<endl;
ofs<<"VERTEX,"<<eBox<<","<<eBox<<","<<sBox<<","<<endl;
ofs<<"VERTEX,"<<sBox<<","<<eBox<<","<<sBox<<","<<endl;
ofs<<endl;
ofs<<"VERTEX,"<<eBox<<","<<eBox<<","<<sBox<<","<<endl;
ofs<<"VERTEX,"<<eBox<<","<<sBox<<","<<sBox<<","<<endl;
ofs<<endl;
ofs<<"VERTEX,"<<sBox<<","<<eBox<<","<<eBox<<","<<endl;
ofs<<"VERTEX,"<<sBox<<","<<eBox<<","<<sBox<<","<<endl;
ofs<<endl;
ofs<<"VERTEX,"<<sBox<<","<<eBox<<","<<eBox<<","<<endl;
ofs<<"VERTEX,"<<sBox<<","<<sBox<<","<<eBox<<","<<endl;
ofs<<endl;
ofs<<"END"<<endl;
ofs<<"]"<<endl;

char str[1024];
char str2[1024];
is.getline(str,1024);
sscanf(str,"%d",&Num);
itoa(Num, NumString, 10);

is.getline(str,1024);

sds.getline(str2,1024);
sds.getline(str2,1024);
```

```cpp
for(int i=0;i<Num;i++)
{
        is.getline(str,1024);
        sds.getline(str2,1024);
        sscanf(str,"%d %f %f %f",&temp,&posx,&posy,&posz);

        tx.push_back(posx);
        ty.push_back(posy);
        tz.push_back(posz);
        sphereStat.push_back(0);
        atomStat.push_back(0);
}

cx.resize(Num);
cy.resize(Num);
cz.resize(Num);
px.resize(Num);
py.resize(Num);
pz.resize(Num);
//count++;
ofs<<"# FRAME      "<<count<<endl;
ofs<<"atoms = ["<<endl;
ofs<<"    ]"<<endl;
ofs<<endl;
ofs<<"obj = box + atoms"<<endl;
ofs<<endl;
ofs<<"cmd.load_cgo(obj,'segment',   "<<count<<")"<<endl;
ofs<<endl;

int test_count = 0;
while(!is.eof())
{
        is.getline(str,1024);
        sds.getline(str2,1024);
        if(strcmp(str, NumString) == 0)
        {
                test_count++;
                cout<<test_count<<endl;
                is.getline(str,1024);
                sds.getline(str2,1024);
                    count++;
          if(count <0 )
                        continue;
       n++;
                ofs<<"# FRAME      "<<count<<endl;
                ofs<<"atoms = ["<<endl;
                cout<<"start processing frame "<<count<<"!"<<endl;
                for(int i=0;i<Num;i++)
                {
                        atomStat[i] = 1;
                        sphereStat[i] = 1;
                }

                for(int i=0;i<Num;i++)
                {
```

```cpp
				is.getline(str,1024);
				sds.getline(str2,1024);
				sscanf(str,"%d %f %f %f",&temp,&nposx,&nposy,&nposz);
				sscanf(str2,"%d %f %f %f",&temp,&posxx,&posyy,&poszz);
				cx[i] = nposx;
				cy[i] = nposy;
				cz[i] = nposz;
				px[i] = posxx;
				py[i] = posyy;
				pz[i] = poszz;
				dis = sqrt((nposx-px[i])*(nposx-px[i])+(nposy-
py[i])*(nposy-py[i])+(nposz-pz[i])*(nposz-pz[i]));

				if(dis>stable && dis<range)
				{

					for(int j=0;j<Num;j++)
					{
						dis2=sqrt((nposx-px[j])*(nposx-
px[j])+(nposy-py[j])*(nposy-py[j])+(nposz-pz[j])*(nposz-pz[j]));
						if(dis2<rad)
						{
							atomStat[i] = 0;
							sphereStat[j] = 0;
							break;
						}

					}


				}
				else
				{
					atomStat[i] = 0;
					sphereStat[i] = 0;
				}
			}
			ofs<<"COLOR,0.000,1.000,0.000,"<<endl;
			int c1=0,c2=0;
			for(int i=0;i<Num;i++)
			{

				if(atomStat[i]==1)
				{
					if(cx[i]<=maxx && cy[i]<=maxy && cz[i]<=maxz &&
cx[i]>=minx && cy[i]>=miny && cz[i]>=minz)
					{
						c1++;

	ofs<<"SPHERE,"<<cx[i]<<","<<cy[i]<<","<<cz[i]<<","<<0.55<<","<<endl;
					}
				}
			}
```

```cpp
                    ofs<<"COLOR,1.000,0.000,0.000,"<<endl;
                    for(int i=0;i<Num;i++)
                    {

                            if(sphereStat[i]==1)
                            {
                                    if(px[i]<=maxx && py[i]<=maxy && pz[i]<=maxz &&
px[i]>=minx && py[i]>=miny && pz[i]>=minz)
                                    {

        ofs<<"SPHERE,"<<px[i]<<","<<py[i]<<","<<pz[i]<<","<<0.55<<","<<endl;
                                            c2++;
                                    }
                            }
                    }
                    ofs2<<count<<" "<<c1<<" "<<c2<<endl;
                    ofs<<"     ]"<<endl;
                    ofs<<endl;
                    ofs<<"obj = box + atoms"<<endl;
                    ofs<<endl;
                    ofs<<"cmd.load_cgo(obj,'segment',   "<<count<<")"<<endl;
                    ofs<<endl;
                    for(int i=0;i<Num;i++)
                    {
                            tx[i] = cx[i];
                            ty[i] = cy[i];
                            tz[i] = cz[i];
                    }
                }
        }
        cout<<count<<" records"<<endl;
        sds.close();
        is.close();
        ofs.close();
        ofs2.close();
        cout<<"done!"<<endl;
        return;
}
```

LAMMPS input file for NEB calculation

```
#innitialization
clear
units metal
dimension 3                    # Dimensions of space for
simulation. 3D is default
newton on on                   # Newton's 3rd law for pairwise and
bonded interactions
#package gpu 0 1 -1

                               # Processors n m o define the proc.
grid
boundary p p p                 # Rules or boundary
atom_style atomic              # Rules for atom styles. Atomic is
default
atom_modify map array sort 0 0.0                         #
atom_modify


variable u uloop 8


# Atom definition



read_data datafile.lammps      # starting stage

lattice bcc 1




#Settings



pair_style eam/fs
pair_coeff * * Fe_mm.eam.fs Fe
```

```
timestep 0.0005


group nebatoms id id1 id2 …..
group nonneb subtract all nebatoms
thermo 100


fix 1 nebatoms neb 1
min_style quickmin



dump 1 nebatoms atom 500 dump.neb.$u
neb 0.0000001 0.00001 500000 500000 1000 final.hop1
```